

# Dynamics of Internal Electric Field Screening in Hybrid Perovskite Solar Cells Probed Using Electroabsorption

Davide Moia<sup>1,2,\*</sup>, Ilario Gelmetti<sup>3</sup>, Philip Calado<sup>1</sup>, Yinghong Hu<sup>4</sup>, Xiaoe Li<sup>5</sup>, Pablo Docampo<sup>4,6</sup>, John de Mello<sup>5</sup>, Joachim Maier<sup>2</sup>, Jenny Nelson<sup>1</sup>, and Piers R. F. Barnes<sup>1,†</sup>

<sup>1</sup>*Department of Physics, Imperial College London, London SW7 2AZ, United Kingdom*


<sup>2</sup>*Max Planck Institute for Solid State Research, Stuttgart, Germany*

<sup>3</sup>*Institute of Chemical Research of Catalonia (ICIQ), Barcelona Institute of Science and Technology (BIST), Tarragona, Spain*

<sup>4</sup>*Department of Chemistry and Center for NanoScience (CeNS), LMU München, München, Germany*

<sup>5</sup>*Department of Chemistry, Imperial College London, London SW7 2AZ, United Kingdom*

<sup>6</sup>*Department of Chemistry, University of Glasgow, Glasgow G12 8QQ, United Kingdom*

 (Received 7 April 2022; revised 16 August 2022; accepted 30 August 2022; published 24 October 2022)

Electric fields arising from the distribution of charge in metal-halide perovskite solar cells are critical for understanding the many weird and wonderful optoelectronic properties displayed by these devices. Mobile ionic defects are thought to accumulate at interfaces to screen electric fields within the bulk of the perovskite semiconductor on application of external bias, but tools are needed to directly probe the dynamics of this process. Here, we show that electroabsorption measurements allow the electric field within the active layer to be tracked as a function of frequency or time. The magnitude of the electroabsorption signal, corresponding to the strength of the electric field in the perovskite layer, falls off for externally applied low-frequency voltages or at long times following voltage steps. Our observations are consistent with drift-diffusion simulations, impedance spectroscopy, and transient photocurrent measurements. They indicate charge redistribution on timescales ranging from 10 ms to 100 s, depending on the device interlayer material, perovskite composition, dominant charged defect, and illumination conditions. The method can be used on typical solar-cell structures and has the potential to become a routine characterization tool for optimizing hybrid perovskite devices.

DOI: [10.1103/PhysRevApplied.18.044056](https://doi.org/10.1103/PhysRevApplied.18.044056)

## I. INTRODUCTION

Metal-halide perovskites combine broad light absorption spectra, good electronic properties, and solution processability, making them promising materials for solar cells [1]. Possibly the most peculiar feature of hybrid perovskite solar cells is the observation of electronic and optoelectronic dynamics that extend to very long timescales (milliseconds to hundreds of seconds) [2,3]. This includes the presence of hysteresis in current-voltage measurements and transient photocurrent measurements, switchable photovoltaic behavior, and huge values of apparent

capacitance [4,5]. Among the explanations for the slow dynamics, the migration of ionic defects within the perovskite layer is now the generally accepted cause [6–9]. While hysteresis effects in hybrid perovskites can be exploited in some other fields [10,11], they remain a concern for solar-cell applications, where a stable and reliable power output upon illumination is desirable. In particular, various reversible but also irreversible performance degradation pathways related to ion motion in perovskite solar cells are reported [12–15]. Recent advances in interlayer engineering, perovskite composition, and crystal growth superficially appear to solve the problem of hysteresis and, in some cases, improve the stability of devices. However, measurements and simulations indicate that an absence of hysteresis does not rule out ionic migration in the cell [16]. Understanding and controlling ion migration in perovskites remains crucial to achieving stable and reliable photovoltaic modules [17].

An equivalent-circuit model recently proposed by some of us, based on ionically gated transistors representing the interfaces between the hybrid perovskite and the contact

\*d.moia@fkf.mpg.de

†piers.barnes@imperial.ac.uk

*Published by the American Physical Society under the terms of the [Creative Commons Attribution 4.0 International](https://creativecommons.org/licenses/by/4.0/) license. Further distribution of this work must maintain attribution to the author(s) and the published article's title, journal citation, and DOI. Open access publication funded by the Max Planck Society.*

layers, can describe most features in the electrical response of hybrid perovskite devices [18]. The model assumes that, when no external bias is applied to the device, the ionic charge carriers (which are also assumed to be the majority carriers) in a perovskite solar cell accumulate at the interfaces to screen the built-in potential due to the difference in work functions of the contact materials [Fig. 1(b)]. Thus, assuming sufficiently large concentrations of mobile ionic defects, only the narrow (relative to the thickness of the active layer) space-charge regions close to the interfaces with the contacts experience a significant electric field. On the other hand, the bulk of the perovskite layer remains almost free of electric field.

If the electrical potential across the device is changed (through application of a bias or generation of a photovoltage) this results in an instantaneous electric field within the perovskite bulk [Figs. 1(c) or 1(d)] that is subsequently screened with a time constant corresponding to the timescale for ionic charge redistribution [Figs. 1(e) or

1(f)]. Ionic redistribution changes the electrostatic potential at the interface and this “gates” the transfer of electronic charge across the interface (recombination or injection processes) in a manner similar to how charge transfer through a bipolar transistor is governed by its base voltage [18].

Although a coherent picture of the underlying device physics is emerging, independent methods to directly interrogate the processes at work are needed. In particular, probes of the electrostatics in the perovskite active layer will help to elucidate the physical process of ionic migration and identify the parameters controlling its dynamics. Measurements of electric field at the surface of exposed device cross sections are reported using Kelvin-probe microscopy or indirectly using electron-beam-induced current measurements [19–22]. While these techniques can give access to the field distribution in devices, their surface sensitivity and resolution can pose challenges to data interpretation [23].

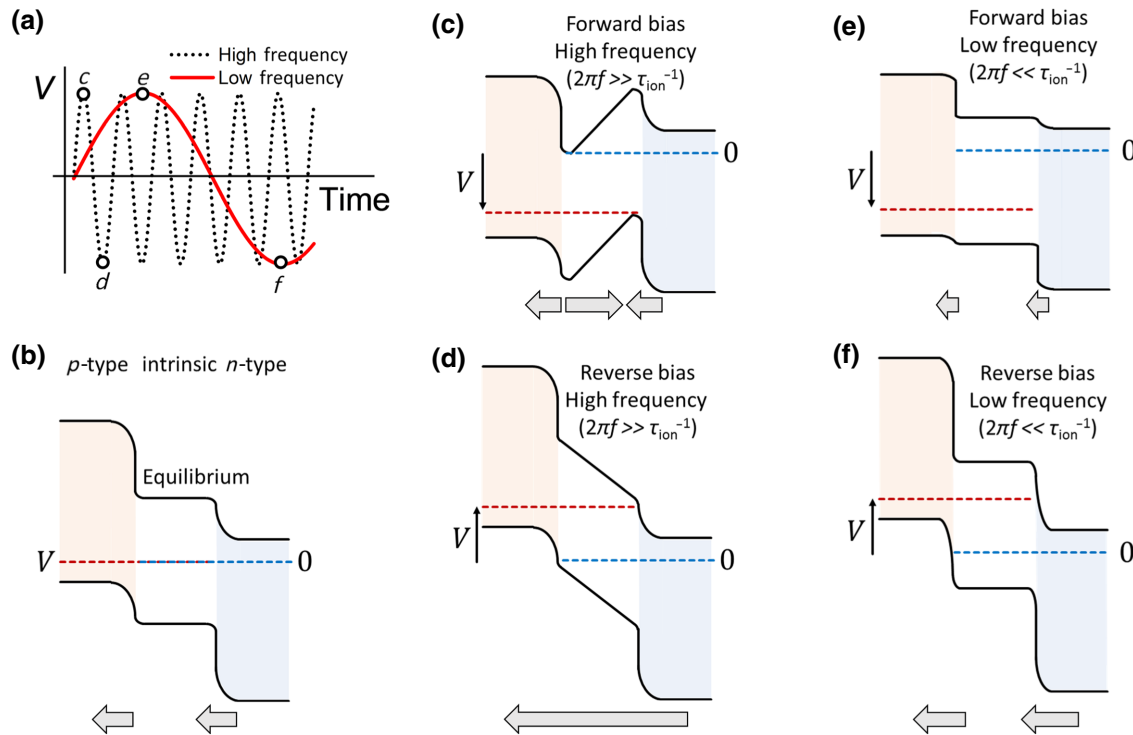


FIG. 1. Schematic energy-level diagrams and electric field direction of a *p-i-n* perovskite solar cell. Schematics show the effect of mobile-ion redistribution, comparing the behavior under applied voltage bias with high or low frequency, as illustrated in (a). (b) Device at zero bias in the dark. *p*-Type, intrinsic, and *n*-type layers are indicated by pink, white, and blue regions, respectively. Hole and electron (quasi-)Fermi levels are indicated by the respective red and blue dashed lines. Resulting energy-level diagrams upon the application of high-frequency voltage for the case of (c) forward bias and (d) reverse bias, or of low-frequency voltage for (e) forward bias and (f) reverse bias. Time constant,  $\tau_{\text{ion}}$ , is associated with ionic redistribution in the perovskite and internal electric field screening. Below each energy-level diagram, arrows indicating the direction of the electric field in the contacts and in the active layer are included. Schematics show approximately flat quasi-Fermi levels in the perovskite layer, corresponding to the high electronic mobility limit (i.e., where the rate of electronic transport is much greater than the rate of recombination and thermal generation in the bulk of the active layer).

Spectroscopic nondestructive techniques are also presented. Electroabsorption (EA) enables changes in optical properties of the materials induced by an electric field to be monitored. Electroabsorption (also referred to as Stark spectroscopy) has previously been applied to hybrid perovskite layers processed in architectures that include one or two insulating layers [e.g., poly (methyl methacrylate), PMMA], in lateral devices, or in solar cells [24–29].

The technique offers insights into the photophysics of charge generation in perovskite solar cells at steady state, as well as the ability to quantify the exciton binding energy and effective mass [25,30,31]. The measured EA signal for methylammonium lead iodide (MAPI) based devices is interpreted in terms of the Stark effect [24,32–35] as well as Franz-Keldysh-Aspnes theory [25,31]. Measurements of EA on complete perovskite solar cells are only explored to a limited extent, with an observed hysteresis in the measured built-in potential value extracted from reflection-mode EA during solar-cell potential scans being attributed to ionic migration by Li *et al.* [34]. EA measurements applied with time or frequency dependence have the potential to give useful information with respect to the dynamics of ion migration and charge distribution in devices. While frequency-dependent EA was recently used to investigate the effect of light intensity on the shape and magnitude of the EA spectrum for MAPI-based devices that included an insulating PMMA layer, [36] the method has not been reported, to date, for solar cells.

In the low-field limit, Franz-Keldysh-Aspnes theory and the quadratic Stark effect predict that an electric field applied to a material will modulate its optical transmittance in proportion to the (energy-dependent) imaginary part of the third-order nonlinear optical susceptibility of the material,  $\chi^{(3)}(h\nu)$ , and can be approximated using superposition of different-order derivatives of the material absorption coefficient [25,29,37–39]. If an electric field,  $F$ , with a static and oscillating component is applied ( $F = \bar{F} + \Delta F \sin[2\pi ft]$ , where  $\bar{F}$  is the steady-state electric field,  $\Delta F$  is the amplitude of the oscillation with frequency  $f$ , and  $t$  is the time), then the transmittance is modulated (due to a periodic variation in the material's dielectric constant):  $T = \bar{T} + \tilde{T}$ , where  $\bar{T}$  and  $\tilde{T}$  are the steady-state and oscillating parts of the transmittance signal. The quantity  $\tilde{T}$  can be split into components varying at the frequency of the applied field,  $\tilde{T}_f$  (the first harmonic), at twice the frequency,  $\tilde{T}_{2f}$  (the second harmonic), as well as higher-order components [see Fig. 2(a) and more details in Sec. II]. The amplitude of the first-harmonic signal,  $\Delta T_f$ , is proportional to the product of the static field and the amplitude of the oscillating component:

$$\frac{\Delta T_f}{\bar{T}}(h\nu) \propto \bar{F} \Delta F \text{Im}[\chi^{(3)}(h\nu)]. \quad (1)$$

The amplitude of the second-harmonic signal,  $\Delta T_{2f}$ , is proportional to the square of the amplitude of the oscillating field:

$$\frac{\Delta T_{2f}}{\bar{T}}(h\nu) \propto \Delta F^2 \text{Im}[\chi^{(3)}(h\nu)]. \quad (2)$$

Regardless of whether Franz-Keldysh-Aspnes theory and/or the quadratic Stark effect represent the underlying physical mechanism relating  $T$  to  $F$ , the form of the relationship described by Eqs. (1) and (2) is expected to be the same. Thus, the relative electric field strength within a perovskite solar cell can be probed by measuring the intensity of the first- and second-harmonic EA signals.

Here, we use frequency-domain and time-resolved EA to investigate the dynamics of the internal electric field, and we observe internal field screening at low modulation frequencies for all perovskite solar cells we measure. The cutoff frequency below which the screening is detected ranges between 10 and 1 kHz, depending on the active-layer material and device architecture measured. We verify the measurements by comparing the frequency of this transition, which corresponds to a timescale of electric field screening, with additional independent experimental techniques: step-dwell-probe (SDP) photocurrent measurements and impedance spectroscopy. We finally show examples of how these techniques can be used to investigate the influence of perovskite morphology, composition, and thickness, as well as the effect of applied dc voltage or light bias. Using these combined spectroscopic and optoelectronic methods, we show a self-consistent multi-method approach that can be directly applied to solar-cell devices and integrated to other routine measurements, such as current voltage and impedance spectroscopy.

## II. METHODS

### A. Device fabrication

Solar cell devices are fabricated on fluorine-doped tin oxide (FTO) substrates and include an oxide (TiO<sub>2</sub> or SnO<sub>2</sub>) interlayer, a hybrid perovskite active layer, a 2,2',7,7'-tetrakis-(*N,N*-di-*p*-methoxyphenylamine)-9,9'-spirobifluorene (spiro-OMeTAD) hole-transporting material, and a semitransparent (~40-nm-thick) gold top contact. Details of the fabrication process are described in Appendix A.

### B. Electroabsorption measurements

Transmission-mode EA spectroscopy is performed on solar-cell devices [Fig. 2(a)]. A xenon lamp is used for continuous probe light. The light beam is passed through a monochromator before being focused onto the active area of the device. The sample is oriented so that the probe light is incident on the metal contact to reduce the intensity of the probe reaching the active layer of the solar

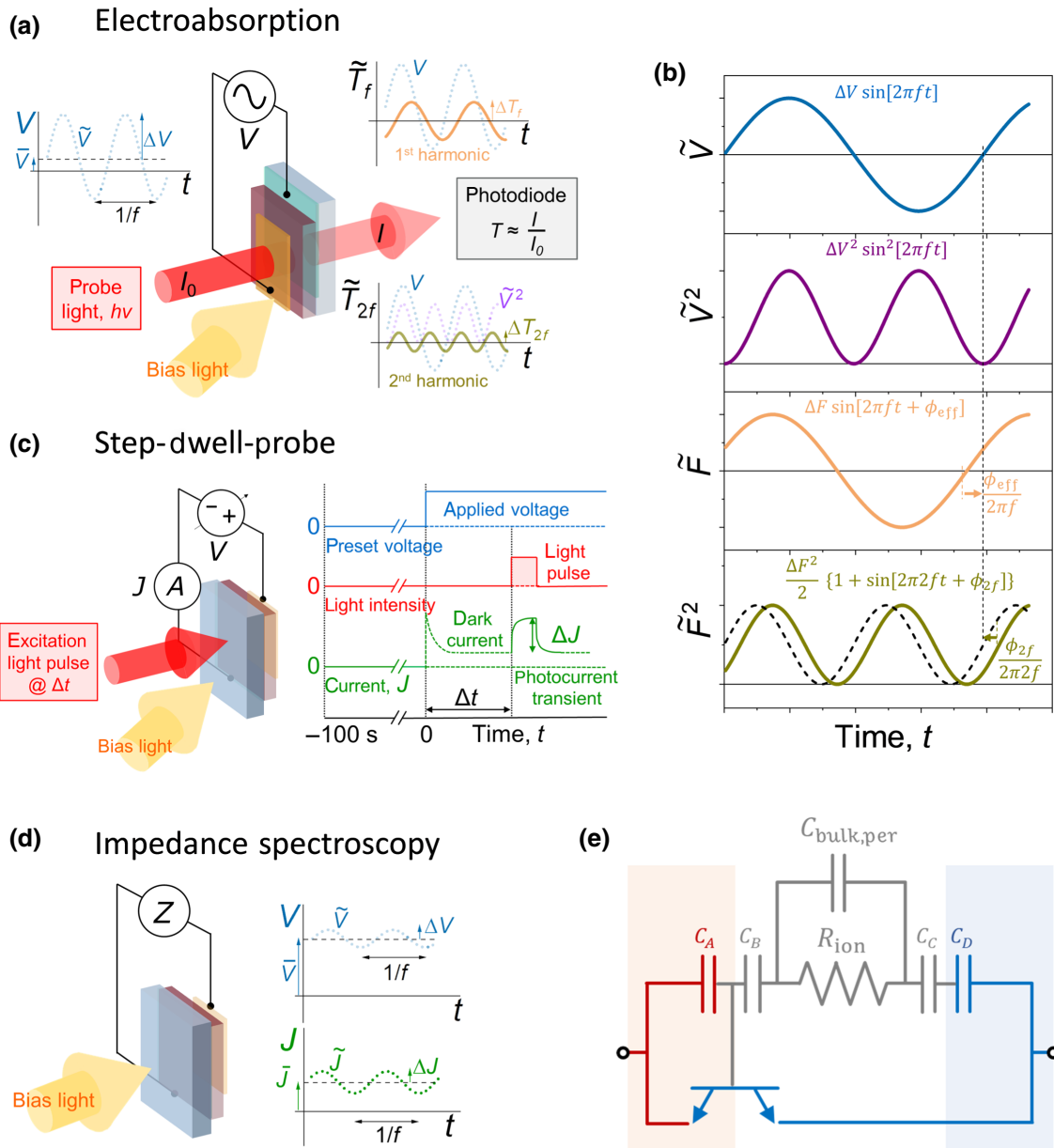


FIG. 2. Schematics for the electroabsorption, step-dwell-probe, and impedance spectroscopy setups. (a) Schematic of the experimental setup and measured photodiode signals in response to an applied voltage ( $V = \bar{V} + \tilde{V}$ ) across the device composed of a static dc component ( $\bar{V}$ ) and a periodic component ( $\tilde{V}$ ) with amplitude  $\Delta V$  oscillating with frequency  $f$ . Intensity of the probe light ( $I_0$ ) transmitted through the sample ( $I$ ) oscillates in response to  $V$ . Two components of the oscillating transmittance ( $\tilde{T}$ ) signal are monitored: the first harmonic, which varies at frequency  $f$  with an amplitude  $\Delta T_f$ , and the second harmonic, which varies at frequency  $2f$  with an amplitude  $\Delta T_{2f}$ . Measurements can be made while the device is illuminated by a bias light. (b) Relative phase between the applied voltage in an EA experiment and the other relevant components: square of the applied voltage,  $V^2$ ; change in electric field,  $\tilde{F}$ , averaged through the perovskite layer, resulting from the applied voltage but reduced by any screening in the device; and average square of the change in electric field,  $\tilde{F}^2$ . Diagram shows the definition of  $\phi_{\text{eff}}$  with respect to the measured phase,  $\phi_{2f}$ , during the second-harmonic measurement.  $\phi_{\text{eff}}$  is representative of the phase lag between the change in field and applied voltage. (c) For step-dwell-probe experiments, the device is left at a preset voltage for  $t < 0$ . Voltage is then stepped to a probe voltage at  $t = 0$ , and photocurrent  $\Delta J$  induced by a light pulse applied to the solar cell after dwell time  $\Delta t$  at the probe voltage is measured. Bias light can optionally be used during measurements. In this study, the bias light (white light-emitting diode, LED) is switched on at  $t = 0$ . (d) Impedance spectroscopy measurements are run on devices in the dark or under light. (e) Equivalent-circuit model used in the analysis of data.

cell. The probe intensity is estimated to be in the order of 0.01 sun ( $\sim 300 \mu\text{W cm}^{-2}$  at 760 nm for measurements of MAPI devices) by measuring the photocurrent of the device and by accounting for a beam size of approximately  $2 \text{ mm}^2$ . The probe beam is then passed through a second monochromator, using filters at the output slit to remove higher-order diffraction components. Finally, the beam is focused on a silicon photodiode connected to the input of a SR830 lock-in amplifier (Stanford Research Systems) or of a HF2LI Zurich instrument lock-in amplifier (the latter is used for frequency-dependent EA measurements). The baseline transmitted signal,  $\bar{T}$ , is recorded before performing the EA measurements by using a chopper at 560 Hz placed between the probe light and the first monochromator and recording the signal from the silicon photodetector through the lock-in amplifier referenced to the external trigger of the chopper. Fractional changes in optical transmission are then calculated as  $\Delta T/\bar{T}$ , as explained below. Two different photodiodes are used for the measurement: a low-noise slow ( $\sim 10 \text{ kHz}$ ) photodetector is used to measure EA spectra at 1 kHz; a second high-speed (5 MHz) photodetector is used for the frequency-dependent measurements from 1 Hz up to 1 MHz. An oscillating voltage with angular frequency  $2\pi f$  applied to the cell is taken from an auxiliary output of the lock-in amplifier ( $\tilde{V}$ ) and combined with a dc voltage ( $\bar{V}$ ) using a custom-made unity gain amplifier circuit to give an output voltage,  $V = \bar{V} + \tilde{V} = \bar{V} + \Delta V \sin[2\pi ft]$ , applied to the solar cell. Values of  $\Delta V \leq 0.8 \text{ V}$  are used to limit injection of electronic charge carriers in the solar cell (which can result in additional charge-induced electromodulation features, see, e.g., Ref. [40]) and to limit degradation of the perovskite mixed conductor. The resulting amplitude of the averaged change in electric field across the solar cells is in the range of  $\Delta F \approx 0.01\text{--}0.06 \text{ MV cm}^{-1}$ , depending on the device and type of measurement.

For the time-domain electroabsorption measurements, a preset dc voltage superimposed on an oscillating voltage ( $\Delta V = 0.5 \text{ V}$  at 1 kHz) is applied to the solar cell via the unity-gain amplifier circuit. After equilibration, the dc voltage is switched to a new value. The first- or second-harmonic EA signal is collected continuously before and after application of the voltage step from the lock-in amplifier (SR830). The time resolution of the measurement is limited by the minimum time constant (typically 100–300 ms) needed to obtain an acceptable signal-to-noise ratio.

### C. Analysis of electroabsorption data

As discussed in Sec. I,  $\tilde{T}$  can oscillate at the fundamental voltage-perturbation frequency,  $f$ , and also at higher-order harmonic frequencies,  $nf$ , where  $n$  is an integer. The time lag of internal screening processes means that changes in electric field can be out of phase with

the applied voltage, which, in turn, is reflected in the phase of  $\tilde{T}$ . Consequently, a phase term must be included when considering the full expression of  $\tilde{T}$ , such that  $\tilde{T} = \sum_{n=1}^{\infty} \Delta T_{nf} \sin[2\pi nft + \phi_{nf}]$ . For the  $n$ th harmonic of the signal at angular frequency  $2\pi nf$ , we can define in-phase and out-of-phase components,  $\Delta T_{nf} \sin[2\pi nft + \phi_{nf}] = \Delta T'_{nf} \sin[2\pi nft] + \Delta T''_{nf} \cos[2\pi nft]$ , with amplitudes  $\Delta T'_{nf} = \Delta T_{nf} \cos \phi_{nf}$  and  $\Delta T''_{nf} = \Delta T_{nf} \sin \phi_{nf}$ , respectively. On this basis, for the first-harmonic measurements,  $\Delta T'_f$  is in phase and  $\Delta T''_f$  is out of phase with the applied voltage. For the second-harmonic measurements,  $-\Delta T''_{2f}$  is in phase and  $\Delta T'_{2f}$  is out of phase with the square of the applied voltage (since  $V^2 \sin^2[2\pi ft] = V^2(1 - \sin[2\pi 2ft + \pi/2])/2$ ).

Therefore, we use  $-\Delta T''_{2f}/\bar{T}$  to illustrate the component of the second-harmonic EA spectrum in phase with the square of the applied voltage. Furthermore, we present the magnitude and phase of the second-harmonic signal as a function of frequency. To give a more intuitive interpretation of the measured second-harmonic signal as it varies with the frequency of the applied potential, we plot the square root of the EA signal, which is proportional to the change in field,  $\Delta F$ , as indicated by Eq. (2). The magnitude corresponds to  $(\Delta T_{2f}/\bar{T})^{1/2}$ , while the resulting effective phase is  $\phi_{\text{eff}} = \phi_{2f}/2 + \pi/4$  (in radians). The phase shift,  $\phi_{\text{eff}}$ , is  $0^\circ$  when the change in absorption (and therefore, the square of the electric field in the active layer) is in phase with the square of the applied potential. If  $\phi_{\text{eff}}$  is nonzero, it refers to a phase shift with respect to the applied voltage. Therefore,  $\phi_{\text{eff}}$  is representative of the phase lag of the electric field in the absorber layer, which oscillates at the frequency of the applied perturbation, as shown in Fig. 2(b). Note that  $\phi_{\text{eff}}$ , as defined above, corresponds to  $\phi_f$  in the simplest case, where  $\bar{F}$  has a sinusoidal profile. This is not expected to be necessarily the case for our experiments, where large values of  $\Delta V$  are used (see Sec. S1 of the Supplemental Material for more details [41]). Nevertheless, defining  $\phi_{\text{eff}}$  still provides insights into the charge-screening effects occurring in the perovskite layer. For all the  $\Delta T/\bar{T}$  results, we account for the fact that data obtained from the lock in is the root mean square of the signal, and we also correct the amplitude of the signal for the trapezoidal shape of  $T$  during the measurement of  $\tilde{T}$  with chopped light.

### D. Optoelectronic transient measurements

SDP measurements [see Fig. 2(c)] are performed using an automated transient optoelectronic measurement rig (TRACER), as described in Ref. [42]. The measurement is described in Ref. [43] and consists of a photocurrent measurement performed with a specific protocol for the voltage bias of the device: the cell is left at a preset voltage (0 V in this work) in the dark for long enough to reach an approximately steady state (between 1 and 100 s, depending on

previous measurements). The device is then stepped to a probe voltage (a positive voltage below the open-circuit voltage,  $V_{OC}$ , in this work) for a particular dwell time, which is long enough to allow complete electronic capacitive charging of the device leaving only the residual dark current. Following this dark dwell time, a LED light pulse of  $6 \mu\text{s}$  is applied to the cell, and the resulting photocurrent during the pulse is recorded  $4 \mu\text{s}$  after application of the pulse [see Fig. 2(c)].  $\Delta J$  is the amplitude and direction (positive or negative) of the corresponding photocurrent pulse. The current-density value averaged between  $6$  and  $2 \mu\text{s}$  before the pulse is subtracted from the total measured value of  $J$  during the pulse to obtain  $\Delta J$ . The sign of  $\Delta J$  is, in part, related to the direction that the internal electric field in the perovskite layer carries the photogenerated charge. The measurements are repeated under the same conditions but with different dwell times, such that a  $\Delta J$  versus dwell-time plot can be obtained. The measurement can be performed with or without an additional bias light (in our case, white LEDs are used). A green LED is used for the pulsed source with an intensity of 2-sun equivalents for devices using methylammonium lead bromide ( $\text{MAPbBr}_3$ ) as the active layer. A red LED with 1-sun-equivalent intensity is used for all other cells. To make sure that the cell is in a comparable state when probing at different dwell times, a control measurement at the shortest dwell time is made before every measurement to check that the inverted photocurrent (negative  $\Delta J$ ) has not changed for this shortest-dwell-time condition.

### E. Impedance spectroscopy

Impedance measurements are performed following the method described in Ref. [18]. In short, a voltage amplitude of  $20 \text{ mV}$  is used for all measurements and a  $1 \text{ MHz}$ – $0.1 \text{ Hz}$  frequency range is used in all cases. For measurements under light bias at open circuit, a chronopotentiometry measurement is performed for  $100 \text{ s}$  to obtain an estimate of the steady-state open-circuit voltage. The device is then left to equilibrate under light (or dark, if applicable) by applying the final voltage measured during chronopotentiometry measurements for a further  $100\text{-s}$  period. The impedance measurement is then made. The impedance spectra are interpreted using the equivalent-circuit model presented in Ref. [18]. The model [see Fig. 2(e)] includes an ionic and dielectric branch (gray elements) and an electronic branch (blue and red elements). The former involves resistor  $R_{ion}$ , representing ionic transport in the perovskite layer. Resistor  $R_{ion}$  is connected on either side to a capacitor associated with the space-charge layer in the contact ( $C_A$  and  $C_D$ ) and a capacitor associated with the space-charge layer or Debye layer in the perovskite ( $C_B$  and  $C_C$ ). The series of two capacitors at either interface represents the total interfacial capacitance and is referred to as  $C_{ion}^\perp$ . The resulting circuit

determines the characteristic time constant,  $\tau_{ion}$  (e.g., assuming symmetrical interfaces,  $C_{ion}^\perp = C_{ion,1}^\perp = C_{ion,2}^\perp$ , one obtains  $\tau_{ion} = R_{ion}C_{ion}^\perp/2$ ). Bipolar transistors are used to approximate the electronic branch. These elements reproduce the gating of injection and recombination currents at the interfaces by the changes in electrostatic potential. In this work, we consider a single transistor associated with the surface-recombination process occurring at one of the interfaces to dominate the electronic component of the measured impedance. Finally, a geometric capacitor,  $C_{bulk,per}$ , is connected in parallel to  $R_{ion}$ . The overall geometric capacitance,  $C_g$ , is determined by the series of all the capacitors described above.

### F. Simulations

Drift-diffusion simulations are performed using the open-source software package Driftdiffusion [44]. Driftdiffusion solves Poisson's equation and the continuity equations for electrons, holes, and mobile ions and the electrostatic potential for a one-dimensional device and their evolution over time. Further details of the simulation methods can be found in Appendix B. We perform simulations of the EA, SDP, and impedance measurements.

## III. RESULTS

### A. Electroabsorption of perovskite solar cells

Figure 3(a) shows EA spectra measured by applying a  $1\text{-kHz}$  sinusoidal voltage of varying amplitude to a MAPI solar cell and probing the changes in optical transmission at the second harmonic of the frequency of the applied potential. Data correspond to the component of the signal that is in phase with the square of the applied voltage. The EA spectra obtained by applying voltage perturbations,  $\tilde{V}$ , with amplitudes  $\Delta V = 0.3, 0.5,$  and  $0.8 \text{ V}$  show the same profile. We observe a quadratic dependence of the EA signal with the applied voltage in this voltage range [see inset in Fig. 3(a)]. Figure 3(b) shows a similar measurement performed using  $\Delta V = 0.5 \text{ V}$  on devices with the same structure but different active-layer thicknesses. The magnitude of the signal increases for thinner active layers, suggesting a correlation of the signal with the average electric field present in the bulk of the material for these devices. The sublinear dependence of the square root of the EA signal versus perovskite thickness suggests a significant drop in field through the contacts and the possibility that most electric field variations occur at the interface with the contacts (see Sec. IV).

We also observe a slight variation of the EA spectral profile for the three devices, which can be ascribed to optical interference effects due to the different thicknesses of the active layer, as discussed in Ref. [25]. Modifications to the line shape can also arise due to field nonuniformity in the active layer, a potentially interesting question for

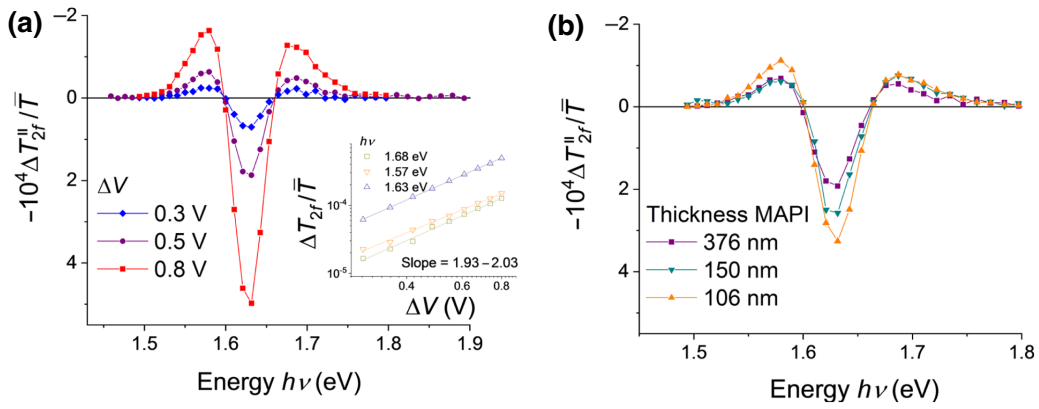


FIG. 3. Second-harmonic electroabsorption of  $\text{TiO}_2/\text{MAPI}/\text{spiro-OMeTAD}$  solar cells measured by applying a sinusoidal voltage at 1 kHz with  $\bar{V} = 0$  V. (a) Effect of different applied-voltage amplitudes,  $\Delta V$ , on second-harmonic  $-\Delta T_{2f}''/\bar{T}$ , plotted as a function of probe-light photon energy,  $h\nu$ , for a solar cell with a MAPI thickness of about 380 nm. Inset in (a) shows a log-log plot of the signal amplitude,  $\Delta T_{2f}''/\bar{T}$ , as a function of  $\Delta V$  for photon energies corresponding to minima ( $h\nu = 1.57$  and  $1.68$  eV) and maxima ( $h\nu = 1.63$  eV). (b) Effect of the MAPI active-layer thickness on the second-harmonic EA for  $\Delta V = 0.5$  V.

future investigation [45,46]. Finally, inherent variations in spectral shape due to changes in average photogenerated charge density in the films due to the probe beam may also occur [36].

The quadratic dependence of the EA signal on the applied voltage is consistent with both Franz-Keldysh-Aspnes and Stark theories, as discussed in previous reports [25,29,45] and in Sec. I. It also suggests that the electric field in the MAPI layer varies in proportion to the applied potential. In the next section, we proceed to investigate the dynamics of the absorber layer's electric field by varying the frequency of the applied voltage ( $\tilde{V}$ ).

## B. Frequency-dependent electroabsorption

Figure 4(a) shows the second-harmonic EA spectra of a MAPI solar cell measured at different frequencies of applied voltage, using a constant amplitude ( $\Delta V = 0.8$  V) and no dc bias ( $\bar{V} = 0$  V). When decreasing the frequency of the voltage perturbation from 1 kHz to 30 Hz, we observe a decrease (with approximately unchanged spectral shape) in the in-phase EA signal and an increase in the out-of-phase EA signal with respect to  $\tilde{V}^2$  [Fig. 4(a)].

By measuring the EA signal at a peak wavelength of 760 nm (1.63-eV photon energy) as a function of applied frequency, we obtain the frequency-dependent EA response in the device. Since we expect the EA signal to be related to the square of the change in electric field in the perovskite, in Fig. 4(b), we show the Bode plot of the square root of the EA measured at 760 nm. The equivalent Nyquist representation of the change in electric field is also displayed in the inset of Fig. 4(b), where we plot  $\Delta F'$  versus  $\Delta F''$ , which are, respectively, in phase and out of phase with the applied potential.

The frequency spectrum of  $(\Delta T/\bar{T})^{1/2}$  in Fig. 4(b) shows a plateau region at intermediate frequencies

(between 100 Hz and 200 kHz), where the effective phase,  $\phi_{\text{eff}}$ , is close to  $0^\circ$ . This is consistent with the field in the perovskite layer being in phase with the applied-voltage perturbation. The signal shows a decrease in magnitude and a phase shift when either high or low frequencies of the applied voltage are used. At high frequencies, we expect the intrinsic  $RC$  time constant of the cell (in the order of  $1 \mu\text{s}$  for the device under consideration) to limit the maximum rate at which the applied potential changes across the solar-cell stack. We therefore ascribe the decrease in magnitude above about 200 kHz to an increasing drop of potential on the series resistance ( $R_s$ ) of the cell and the capacitive charging of the geometric capacitance associated with the high-frequency dielectric properties of the whole device stack ( $C_g$ ). In the low-frequency region (for  $f < 100$  Hz), a process with slow dynamics appears to screen the internal electric field in the active layer, thus decreasing the EA signal, also consistent with data in Fig. 4(a). In Sec. IV we discuss the nature of this screening process, which appears to be due to ionic charge migration. Notably, based on the approximately unvaried spectral shape detected at different frequencies shown in Fig. 4(a), we ignore potential distortion in the electromodulated spectral shape of the second-harmonic signal due to inhomogeneity in the field distribution within the active layer. Such distortion can potentially lead to a reduction in the magnitude of the EA peak monitored at 1.63 eV at low frequency, due to an increase in electric field nonuniformity in the active layer [45,46]. While different in its physical origin, such an effect can also be associated with electric field screening in the bulk of the active layer. To validate the observation described in Fig. 4, in the next section, we compare the frequency-dependent EA results with two other independent techniques.

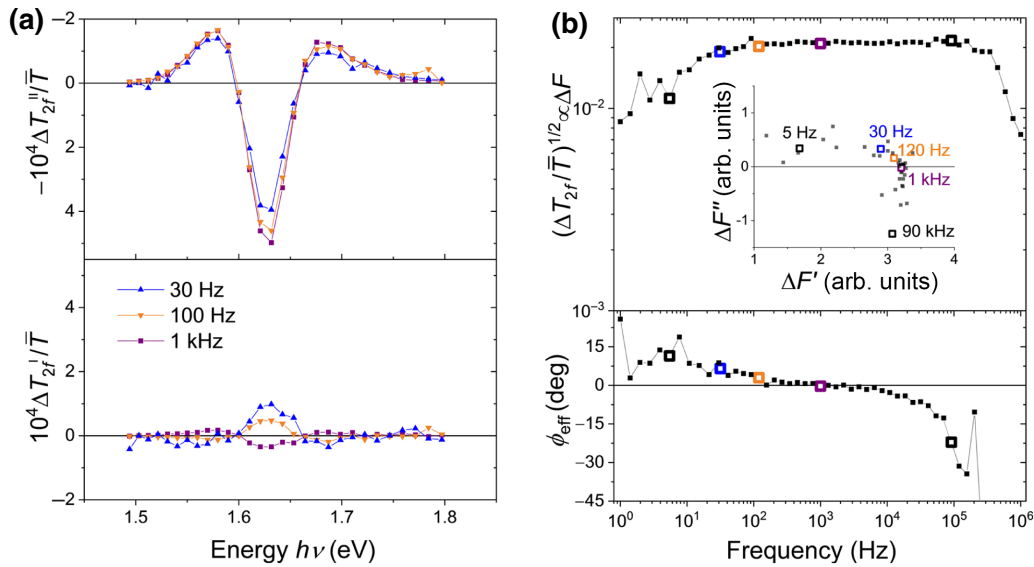


FIG. 4. Frequency-dependent electroabsorption measurement on a solar cell with  $\text{TiO}_2/\text{MAPI}/\text{spiro-OMeTAD}$  architecture. (a) Second-harmonic EA spectra recorded at different frequencies of applied voltage ( $\Delta V = 0.8$  V). Top and bottom panels refer to the components in phase and out of phase with the square of the applied potential, respectively [see Fig. 2(b)]. (b) Bode plot of the square root of the EA peak at 1.63-eV photon energy (760 nm) measured at different frequencies. Inset in (b) shows the equivalent Nyquist representation of the change in electric field in the perovskite using frequency as an implicit parameter. Phase  $\phi_{\text{eff}}$  is calculated as  $\phi_{\text{eff}} = \phi_{2f}/2 + \pi/4$  (see Sec. II).

### C. Measuring electric field screening using electroabsorption, step-dwell-probe, and impedance spectroscopy

Figure 5 shows five different measurements of a  $\text{TiO}_2/\text{MAPI}/\text{spiro-OMeTAD}$  solar cell in the dark (for EA experiments, a weak probe light is applied, see Sec. II). Figure 5(a) compares frequency-dependent EA data from Fig. 4(b), with SDP data where the photocurrent is plotted against the reciprocal of the dwell time,  $\Delta t$ . This is done to compare the estimated timescales of electric field screening on the frequency scale. Finally, the capacitance extracted from the impedance of the cell is shown.

The three measurements highlight the spectroscopic, optoelectronic, and electrochemical responses of the device. Data from each measurement show two frequency regions with different behavior, a high-frequency region (fast timescale, white background in Fig. 5) and a low-frequency region (long timescale, purple background in Fig. 5):

(a) Electroabsorption: an approximately constant EA signal is observed in the 100 Hz–100 kHz region, with a drop in signal magnitude for  $f < 10$ –100 Hz. This is consistent with (partial) screening of the electric field [see  $\vec{F}$  in Fig. 5(c)] by ionic charges occurring at low frequencies.

(b) Step-dwell-probe: the photocurrent induced by a light pulse incident on the cell at different times after the application of a step potential [see direction of electron transport and hole transport in Fig. 5(c)] is positive

(charges moving away from their respective selective contact) for  $\Delta t < 0.1$  s and changes sign for light pulses applied at later times. This is consistent with changes in direction for the driving force (affected by the electric field in the perovskite layer) of the photocurrent [43,47].

(c) Impedance spectroscopy: for high frequencies, the capacitance of the solar cell remains constant, which we attribute to the geometric capacitance contribution. Its value increases for  $f < 10$ –100 Hz due to ion redistribution within the perovskite active layer [see electronic charge accumulating at the contacts and change in ionic distribution in Fig. 5(c)].

For each technique, we highlight the transition in behavior described above by defining a parameter,  $f_0$ , to be the frequency (or inverse dwell time for SDP measurements) that divides the high-frequency “plateau” from the low-frequency electric-field-screening regime. We extract  $f_0$  as the frequency value obtained from the intersection between a (constant) line fitted to the high-frequency plateau and a line fitted to the transition to low-frequency behavior (see black dashed lines in Fig. 5). While the type and degree of perturbation is different among the three techniques, we observe a very similar trend and similar estimates of  $f_0$  at which we expect the electric field screening to occur. Notably,  $f_{0,C}$  is not strictly associated with the low-frequency impedance time constant. However, it is easily accessible and seems to correlate qualitatively with the results from other techniques. In Fig. 5(a), we also include results from simulations obtained using the



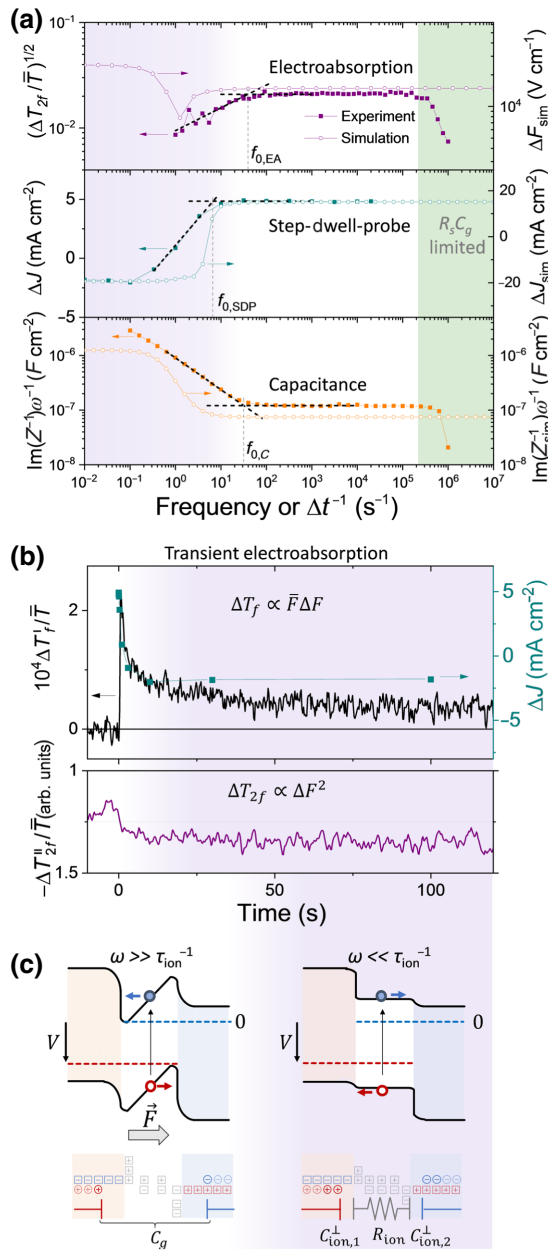


FIG. 5. Frequency and time-resolved techniques measuring the dynamics of electric field screening for a MAPI solar cell in the dark. (a) Experimental data and drift-diffusion simulation results of frequency-dependent EA, SDP vs inverse dwell-time ( $\Delta t^{-1}$ ) and capacitance extracted from impedance. The green area indicates the limitations due to series resistance and geometric capacitance  $R_s C_g$ . Values of  $f_0$  are obtained from the intersection of fitting lines to the high-frequency region and to the transition to the low-frequency region. (b) In-phase 1<sup>st</sup> harmonic (top) and 2<sup>nd</sup> harmonic (bottom) transient EA signal at 760 nm on application of a voltage step,  $\bar{V} = 0 \text{ V} \rightarrow 0.5 \text{ V}$ , at  $t = 0 \text{ s}$  superimposed on  $\tilde{V}$  ( $\Delta V = 0.5 \text{ V}$  and 1 kHz). Dwell-time dependent SDP data shown in (a) are superimposed on the 1<sup>st</sup> harmonic transient. (c) Energy-level diagrams for the early (white background) and long-timescale (purple background) response to a voltage step, and implications in terms of electric field, photocurrent direction, and charge distribution.

Drift-diffusion software [44], where we simulate the EA, SDP, and impedance measurements on a solar-cell stack with representative parameters (Appendix B). The general trend discussed above is well reproduced, with a high-frequency response that can be attributed to the dielectric properties of the simulated device without the contribution of ion transport, and a low-frequency behavior that matches the electric-field-screening effect due to the redistribution of mobile ionic defects. Discrepancies observed between experimental and simulated data are due to the simplified system considered for the simulations, which assume nondispersive transport and a single mobile ionic species. For  $\Delta F_{sim}$ , which is representative of the simulated EA signal, we observe an increase in magnitude for frequencies below 1 Hz, a frequency region that cannot be resolved experimentally. We provide more detail on this and further simulated results in Sec. S2 of the Supplemental Material [41], where we show that the increase in the low-frequency simulated signal is obtained when using similar (or larger) values of the interfacial capacitance on the contact side to that on the perovskite side (e.g.,  $C_C \approx C_D$  for the simulations in Fig. 5).

To investigate the very-low-frequency behavior of devices further, we develop a time-resolved transient EA technique. Figure 5(b) shows an experiment performed on the same type of solar cell as that described in Fig. 5(a), where we apply a voltage  $V = \bar{V} + \tilde{V}$  and measure the first- or second-harmonic signal at 760 nm as a function of time following a step change in  $\bar{V}$ . While in the previous EA experiments we kept  $\tilde{V} = 0 \text{ V}$  throughout the measurement, here we apply a step in the dc voltage such that  $\bar{V} = 0 \text{ V}$  for  $t < 0 \text{ s}$  and  $\bar{V} = 0.5 \text{ V}$  for  $t > 0 \text{ s}$ . An oscillating voltage ( $\tilde{V}$ ) with  $\Delta V = 0.5 \text{ V}$  at 1 kHz is superimposed on the step potential to allow the evolution of field to be monitored using the lock-in technique. As shown in Fig. 5(b) (top graph), the change in absorption related to the first harmonic due to the step potential presents a sharp peak at early times ( $t < 1 \text{ s}$ ) and tends to stabilize over a timescale on the order of 10–100 s. In the same figure, we also include SDP data from Fig. 5(a) for comparison of the long-timescale response between the two techniques. This result, combined with the observations above, shows that the process of electric field screening occurs over a large range of timescales. After decay, the baseline in the measurement also shifts slightly, suggesting a detectable change in  $\bar{F}$  at long timescales (after the screening process) on application of the forward bias [see Eq. (1)].

When the  $\tilde{V}$  step is reversed, the time-resolved signal is inverted (Appendix C), as would be expected since Eq. (1) predicts that the EA signal depends on the sign of  $\vec{F}$ . We note that the first-harmonic EA spectrum for MAPI solar cells shows a similar shape to that of the second-harmonic spectrum [as expected from Eqs. (1) and (2)]. According to Eq. (1), the detection of a nonzero signal for the first-harmonic measurement, even for  $\tilde{V} = 0 \text{ V}$ ,

implies the presence of a steady-state electric field in the solar cell's active layer. This is consistent with space charges forming at the interfaces with the contacts (see simplified schematics in Fig. 1). In Ref. [48], noncentrosymmetry of the halide perovskite is discussed as an important factor to explain the detection and  $\bar{V}$  dependence of the first-harmonic EA measurements. Similar behavior for first-harmonic measurements to that shown in Fig. 5(b) is observed for different active-layer compositions (see Appendix C). On the other hand, a much larger change in baseline at long timescales is observed for transient EA measurements on MAPI solar cells with SnO<sub>2</sub> contacts (Fig. S11 within the Supplemental Material [41]). Following a peak in the data at early timescales similar to the one in Fig. 5(b), these cells show a long-time baseline change that is opposite to the case with TiO<sub>2</sub>. We check that this measurement is not affected by electroluminescence contributions (Fig. S12 within the Supplemental Material [41]). This result cannot be explained on the basis of the interpretation presented in this study. As a general note, the analysis of the first-harmonic EA signal is complex, because of changes in spectral shape over several measurements, possibly due to additional contributions from other induced absorption features (see Appendix C). We also find that changes in the magnitude and sign of the first-harmonic signal vary over very long timescales. This makes it difficult to perform, for example, frequency-dependent first-harmonic EA measurements. The second-harmonic EA yields more consistent results, especially for TiO<sub>2</sub>/MAPI/spiro-OMeTAD cells, showing almost identical spectra for measurements on the same device run over several days and across different devices. The frequency-dependent EA on these solar cells is also generally reproducible, with some variability from sample to sample (see, for example, Fig. S21 within the Supplemental Material [41]).

The transient EA measurement for the second-harmonic signal [bottom graph of Fig. 5(b)] does not present a clear peak at  $t = 0$  s like the one observed for the first-harmonic measurement. Instead, data show a small step, followed by a very slow variation occurring over similar timescales to the slow transient of the first-harmonic signal. The absence of a peak is consistent with Eq. (2) (second-harmonic signal is independent of  $\bar{F}$ ). The increase in signal magnitude upon application of the forward bias is likely to be due to the increase in the capacitance of the contacts at forward bias, which increases the fraction of applied  $\bar{V}$  dropping across the absorber layer during measurements. On the basis of these considerations, the dependence of the EA signal on the applied dc voltage (see Appendix D) can provide information on the voltage dependence of the capacitances involved in the cell.

The consistency between the results obtained via these different techniques shows that each can be used to probe the timescale of electric field screening within the active

layer of perovskite solar cells. These tools are, therefore, suitable to test the effect of different optical bias and device parameters on this process, as we show in the next section.

#### D. Effect of bias light; interlayers; and absorber film thickness, morphology, and composition

We perform EA, SDP, and (apparent) capacitance measurements on a number of different device architectures under both dark and a range of bias-light conditions. Figure 6 shows a summary of these measurements and the frequencies at which the field-screening transition,  $f_0$ , occurs. First, we describe the observed changes in dynamics for each measurement technique when the device is exposed to bias light with respect to measurements performed in the dark. Figure 6(a) shows that, for all measurements on the reference solar cell (TiO<sub>2</sub>/MAPI(360 nm)/spiro-OMeTAD), the field-screening transition shifts to higher frequencies as the bias-light intensity increases. The corresponding values of  $f_0$  are shown in Fig. 6(b), where the increasing trend with light can be observed (ranging between 1 and 10<sup>4</sup> Hz). The values of  $f_{0,EA}$  and  $f_{0,C}$  show close agreement, while the values for  $f_{0,SDP}$  show a similar trend with light intensity but with an offset to lower frequencies; this offset is likely to be intrinsic to the technique, resulting from a time lag required before sufficient ionic redistribution has occurred to start influencing the photocurrent direction. The latter is sensitive to the direction of the quasi-Fermi-level gradient rather than the field only. Figure 6(a) also shows that the abruptness of this transition for SDP data is reduced by bias light, with the appearance of a high-frequency decay in photocurrent to about 0 mA cm<sup>-2</sup>, followed by the roughly unchanged low-frequency transition to negative photocurrent values (for more examples for other device structures, see Sec. S4 of the Supplemental Material [41]).

When the first harmonic of EA is monitored following a potential step, we observe that the initial, rapidly changing, component of the signal can no longer be resolved as the bias-light intensity is increased [Fig. 6(c)]. Consistent with the observations in Fig. 6(a), the slow-timescale component of the first-harmonic signal remains at all light intensities. Figure 6(d) shows the values of  $f_0$  extracted from measurements on other device architectures and active-layer thicknesses (impedance and current-voltage curves of the devices can be found in Secs. S7 and S8 of the Supplemental Material [41]). In all cases,  $f_0$  increases with increased light intensity, implying more rapid field screening. The perovskite-layer thickness appears to have a relatively weak influence on  $f_{0,EA}$  or on the dynamics of the long-timescale measurements (see Figs. S20 and S25 within the Supplemental Material [41]). As we discuss below, the contribution of the probe light and different surface-recombination performances for devices with different thicknesses can explain this observation. The value

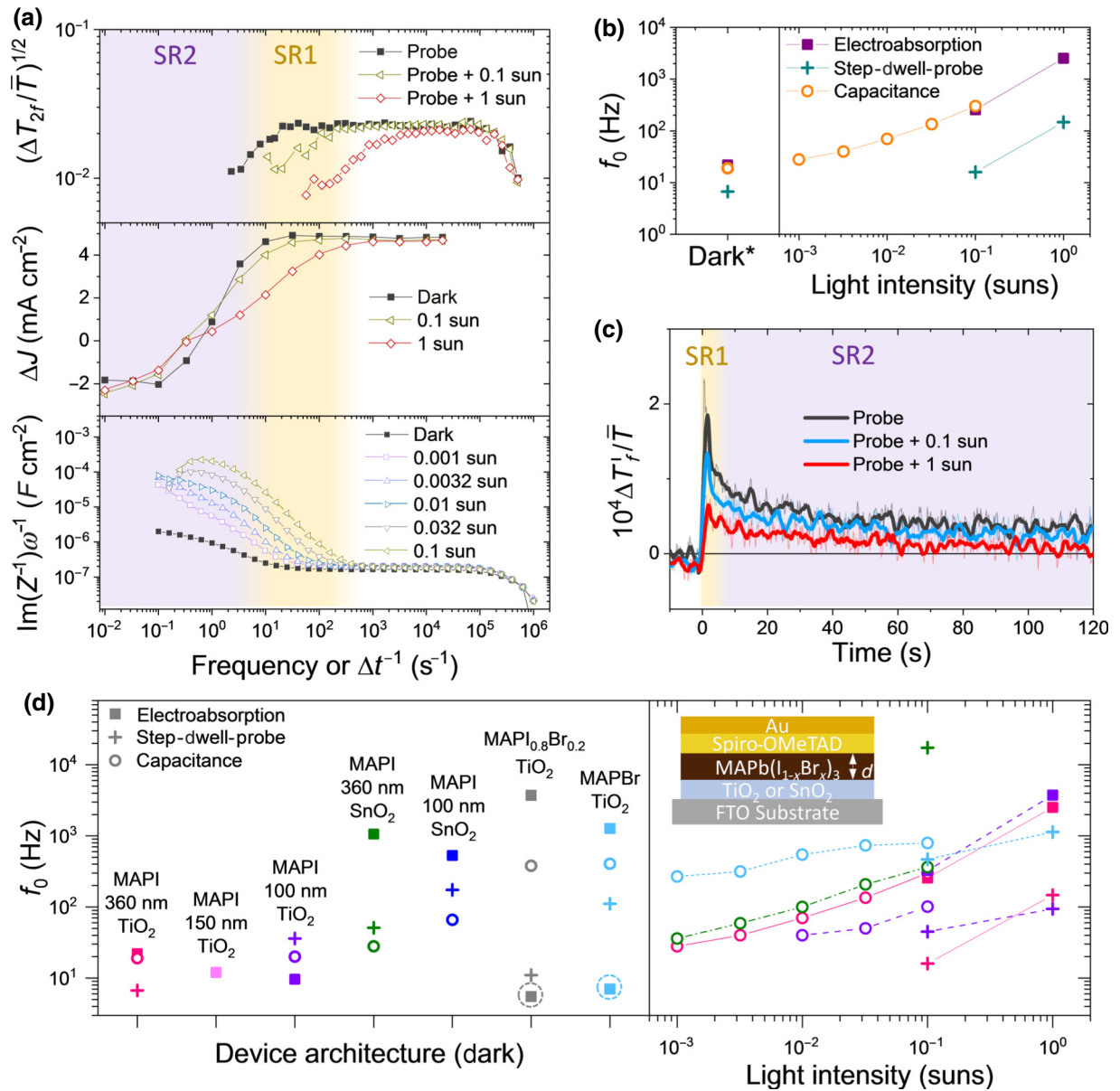


FIG. 6. Effect of different solar-cell parameters on electroabsorption, step-dwell-probe, and capacitance measurements. (a),(c) Measurements on TiO<sub>2</sub>/MAPI/spiro-OMeTAD solar cells, as in Figs. 5(a) and 2(b), also showing the effect of light on  $f_0$  (MAPI thickness 360 nm). Purple and yellow backgrounds indicate the approximate frequency range of screening regime 1 (SR1, observed only under illumination) and screening regime 2 (SR2, observed under dark and light conditions). In (c), smoothed data (15 points,  $\sim 3$  s window) are shown superimposed on raw data. (b) Values of  $f_0$  extracted from data plotted in (a). (d) Summary of data obtained in the dark (left) and under light (right) for solar cells with different architectures. Inset of (d) shows the device structure and parameters investigated in this study: interlayer material, hybrid perovskite composition, and thickness  $d$ . Circled data points indicate an additional characteristic frequency extracted from the EA of some devices. \* For EA data measured without bias light, the cell is exposed to a weak probe light (see Sec. II).

of  $f_{0,C}$  is also insensitive to the change in thickness, which is expected, given the counteracting effects of increased ionic resistance and decreased geometric capacitance on increasing active-layer thickness (see below). Only values of  $f_{0,SDP}$  show an appreciable increase with decreasing layer thickness. In Sec. S5 of the Supplemental Material [41], we also show that  $f_{0,EA}$  is not influenced by very

different MAPI-layer morphologies, suggesting a negligible contribution of grain boundaries to the screening dynamics probed with EA.

In contrast, the electron-transporting material (ETM) appears to have a significant influence on  $f_0$ . When TiO<sub>2</sub> is replaced by SnO<sub>2</sub>, the values of  $f_0$  increase by up to 50 times, depending on the measurement and device

[Fig. 6(d)]. A lower capacitance at high frequencies for SnO<sub>2</sub> compared to TiO<sub>2</sub>, consistent with the trend in  $f_{0,C}$  (Fig. S18 within the Supplemental Material [41]), can explain this effect (see also next section). We note that measurements on devices with SnO<sub>2</sub> as the ETM show lower reproducibility compared with the TiO<sub>2</sub> case, in terms of EA signal magnitude and frequency-dependent EA spectral shape (see Figs. S16–S18 within the Supplemental Material [41]). Nevertheless, a relatively large value of  $f_{0,EA}$  is consistently observed for all devices with SnO<sub>2</sub>. Changing the hole-transporting material, spiro-OMeTAD doped with lithium ions, to undoped spiro-OMeTAD does not significantly influence  $f_{0,EA}$  (Fig. S22 within the Supplemental Material [41]). This observation suggests that lithium ions are not directly involved in the screening behavior at the frequencies monitored in this experiment.

Finally, Fig. 6(d) also shows the influence of changing the perovskite-layer composition. For the frequency-dependent EA spectrum of MAPbBr<sub>3</sub> or MAPb(I<sub>0.8</sub>Br<sub>0.2</sub>)<sub>3</sub> (see Appendix E), we identify a mild decrease in signal for frequencies below about 1 kHz, followed by a sharp drop below about 10 Hz. In Fig. 6(d), we indicate both these frequencies (the latter is highlighted by a dashed circle). Higher values of  $f_0$  for MAPbBr<sub>3</sub> compared to MAPI are also recorded using SDP and capacitance measurements. We also record an increase in  $f_{0,SDP}$  with light for this device, similar to MAPI cells, while we observe a drop in signal magnitude but no clear shift for  $f_{0,EA}$  to higher frequencies when illuminating the MAPbBr<sub>3</sub> cell. More complex behavior for MAPb(I<sub>0.8</sub>Br<sub>0.2</sub>)<sub>3</sub> is observed under light with a nonmonotonic drop in signal with decreasing frequencies (see Appendix E). We also perform measurements on mixed-cation hybrid perovskite solar cells. In Appendix E, we show that, for all compositions containing between two and four different *A* cations, the value of  $f_{0,EA}$  in the dark increases to about 1 kHz compared to the case of MAPI on TiO<sub>2</sub> (100–200 Hz). This effect is present regardless of using TiO<sub>2</sub> or SnO<sub>2</sub> as the interlayer (Fig. 15).

## IV. DISCUSSION

### A. Interpretation of measurements in the dark

The frequency- and time-dependent EA techniques that we developed allow a direct measurement of the timescale for electric field screening in the metal-halide perovskite layers of solar cells. The results show good qualitative agreement with indirect measurements of this field-screening process inferred from SDP photocurrent measurements and impedance spectroscopy measurements. These screening dynamics depend on the details of the device architecture, composition, and operation. We now discuss possible interpretations of the screening mechanisms based on the experimental observations reported in this work.

The field screening that we observe is likely to be due to redistribution of ionic charge in the hybrid perovskite layer. This is consistent with many previous reports suggesting that ion transport in these photovoltaic materials is responsible for the slow optoelectronic dynamics observed in solar-cell devices, resulting in behavior such as current-voltage hysteresis [6,7,16,18,49]. Our observations are consistent with this interpretation, also discussed by Rana *et al.* [36], and provide a direct nondestructive measurement of field screening within the active layer of complete devices. Specifically, Ref. [36] considers MAPI-based devices including an insulating PMMA layer, for which a drop in EA signal intensity at low frequency is detected only for large enough probe intensities. When using low probe intensities, no significant change in signal is instead detected in the range between 40 Hz and 1 kHz, stressing the critical role of light, even at relatively low intensities. We also note that larger applied fields are considered in Ref. [36] (0.3 MV cm<sup>-1</sup>) compared to our investigation, which may affect the screening behavior of the mobile ionic defects and the relative contribution of injected electronic carriers.

Device architecture can influence the screening timescale. When device contact materials are changed, there is an associated change in the capacitance of the interfaces [ $C_{ion}^\perp$ , see also Fig. 5(c)] which leads to a change in the ionic screening time of the device ( $\sim R_{ion} C_{ion}^\perp / 2$  for the symmetrical case), assuming that electrode polarization dominates such dynamics. For example, a lower doping density in SnO<sub>2</sub> relative to TiO<sub>2</sub> would lead to a smaller capacitance, and thus, shorter screening time. Active-layer composition can similarly influence both the capacitance of the interfaces (due to defect density, energetic offset, and dielectric constant, all of which would influence space-charge layer widths, and thus, capacitance) and ionic resistance (due to different mobile defect concentrations and mobility). A further contribution from electronic charge carriers cannot be ruled out, as we discuss below.

### B. Electric field screening under light

We now consider the effect of light on the measured characteristic frequency of electric field screening. Clearly, the techniques used in this study offer different probes with different sensitivity to electric field screening and, especially for the case of measurements under light, they point towards complex, possibly multiprocess, behavior. When light is applied to the reference device structure, TiO<sub>2</sub>/MAPI/spiro-OMeTAD, we observe a pronounced shift to higher values of frequency  $f_0$ , below which field screening is “activated” [Figs. 6(a) and 6(b)]. We refer to this behavior under light and the frequency range where it occurs as SR1. This effect is also visible from time-resolved transient EA measurements [smaller initial amplitude of the signal at early timescales for cells under

illumination, Fig. 6(c)]. At longer times, following a voltage step for the time-resolved EA and SDP measurements, a second slower component to the change in electric field is also detected, the rate of which is relatively uninfluenced by light. We refer to this as SR2. The light independence of SR2 is also displayed by the similar transient dynamics observed for time-resolved EA measurements, where the bias light is switched on or off, while keeping  $\bar{V}$  unchanged (see Fig. S19 within the Supplemental Material [41]). For impedance measurements, the appearance of SR1 can be associated with the increase in apparent capacitance under light at low frequencies, which increases the value of  $f_{0,C}$  [18]. As mentioned above,  $f_{0,C}$  does not have an intuitive physical meaning, and it is used here to track the changes in magnitude and/or dynamics of the low-frequency capacitance component (see Appendix F). We note that, because the use of a probe light is necessary to carry out EA measurements, it is not possible to evaluate  $f_{0,EA}$  for the completely dark case. Based on the trend discussed above, the value of  $f_{0,EA}$  extracted from measurements without bias light may be affected by the probe light intensity, as also reported by Rana *et al.* [36]. Different average charge densities induced by the probe light in different devices can potentially contribute to some of the observed trends in  $f_{0,EA}$  as a function of active-layer composition and ETM, as discussed below (see also Sec. S8 of the Supplemental Material [41]). In this context, the comparison in Figs. 5 and 6 of EA data with the results obtained from the other techniques, for which measurements in the dark are possible (here SDP and impedance), is particularly useful.

The two regimes of electric field screening, SR1 and SR2, detected by these techniques highlight the possibility for two processes with different dynamics and different dependence on illumination to occur. These processes can be electronic or ionic in nature. Regarding electronic charge carriers, an additional contribution to electric field screening from photogenerated charges and injected charges needs to be considered. As for the ionic contribution, it is well established that iodide vacancies are the majority carriers in MAPI [6,7]. Lower diffusion coefficients are evaluated for methylammonium cations and other defects, which may also provide a further screening ability [50–52].

In the first scenario, SR1 can be due to injected and photogenerated electronic charges redistributing in the cell to screen the electric field induced by the externally applied potential. SR2, which is similar between measurements on the same device irrespective of the illumination level, may be related to ionic relaxation, e.g., due to redistribution of iodide vacancies. Analysis of simulations suggest that electronic screening, while active at faster timescales compared to experiments, is present and increases in magnitude under light because of the contribution from the photogenerated electronic charge carriers (see Sec. S2 of the Supplemental Material [41]). Furthermore, we

test the frequency-dependent EA for a TiO<sub>2</sub>/MAPI/spiro-OMeTAD device by including a dc offset,  $\bar{V} = 0.5$  V, to the applied ac voltage. We observe a slight drop in the signal at frequencies below about 500 Hz (Appendix D), which is consistent with an increase in the background electronic concentration in the device. This would suggest that electronic currents are playing some role in the fast component of the screening process. This effect may also be related to the accumulation of photogenerated charge in trap states, which is not accounted for explicitly in our simulations at present (transport is described by constant electronic mobilities of typical magnitude [53]). Trapping of electronic charges can explain the observation of relatively low values for  $f_0$  (kHz range) observed under light for some of the devices investigated here. We also emphasize that screening can lead to a decrease and to an increase of the EA signal magnitude, depending on the ratio between the interfacial capacitance on the perovskite and on the contact side, as shown for the very-low-frequency simulated EA data in Fig. 5(a). Such aspects can explain the different EA behavior observed for solar cells under light with TiO<sub>2</sub> or SnO<sub>2</sub> as electron-transporting-layer materials (Fig. S16, see Sec. S2 of the Supplemental Material for discussion [41]). We note that ionic redistribution may also contribute to faster screening at high-bias-light intensity (SR1) based on the possible increase in ionic conductivity under light, which is reported to be relevant for iodide defects [54–56]. The long-timescale behavior (SR2) can then also be related to a second ionic species, which is comparatively unaffected by the background light intensity [57]. A detailed investigation of these screening effects deserves future work.

### C. Spatial distribution of the electric field

We now comment on the spatial distribution of the changes in electric field that we measure. The fact that the magnitude of the second-harmonic EA signal scales with the square of the applied potential (with some fluctuation; this is the case for all devices, see Fig. S23 within the Supplemental Material [41]) suggests that the square root of the EA signal might be used to evaluate the electric field strength in the active layer. However, the weak dependence of both signal magnitude and some of the time constants extracted from the measurements on active-layer thickness indicates a more complex situation. Regarding the thickness-dependent magnitude of the EA signal at high frequencies, we note that the contribution to the EA signal will be more significant from the regions of the device where the active layer is thinnest (because of the large electric field in those regions for a certain applied high-frequency voltage). It follows that, if the surface roughness of the active layer were to increase superlinearly with thickness, this could also contribute to the trend shown in Fig. 3(b). The thickness dependence of the EA signal

magnitude is also consistent with only a small fraction of the changes in potential dropping in the active layer, while a large fraction of it drops across the contact materials (see Secs. S2 and S9 of the Supplemental Material [41]). It is also possible that, if screening were fast enough within the active layer bulk, most of the potential drop would be confined to its interfaces (e.g., across the depletion layer at the MAPI/TiO<sub>2</sub> interface [58]). A mixed situation between the cases described above is likely.

#### D. Screening dynamics and photovoltaic response

We briefly discuss to what extent the electric field screening dynamics can be further evaluated in relation to device performance. Our simplified model already shows how such a relationship can be rather complex. Parameters such as the contact materials and active-layer composition influence the screening dynamics, as discussed above, but also most processes that are key to the photovoltaic function, such as bulk and surface recombination, charge extraction, and light harvesting efficiency, to name a few.

While a general relationship between the screening dynamics and device performance cannot be drawn, we can identify some correlations between these two aspects and discuss potential causality questions. First, we relate the values of  $f_0$  extracted in our study and the hystereses of current-voltage curves measured for the same solar-cell structures under 1 sun at a scan rate of about 0.1–0.2 V s<sup>-1</sup>. Here, we consider  $f_0$  measured in the dark (once again, for EA measurements, a probe light is used), to focus our attention on the ionic contribution. From data in Fig. 7(a), where  $f_0$  values are plotted against the hysteresis index of devices, as defined in Ref. [59], we highlight the following points. An overall inverse correlation is found between the hysteresis index and the lowest value of  $f_0$  measured for each device. For solar cells with TiO<sub>2</sub> as the ETM, we find generally higher hysteresis indexes at the selected scan rate than for cells using SnO<sub>2</sub>. As discussed above, this may be due to the low interfacial capacitance associated with the perovskite-SnO<sub>2</sub> interface. This allows for faster screening dynamics, implying the ability of the device to “follow” the voltage scan at a faster rate compared with devices using TiO<sub>2</sub> as the ETM. For almost all cells with TiO<sub>2</sub>, at least one of the values of  $f_{0,EA}$  extracted for each device is as low as  $f_{0,SDP}$  and  $f_{0,C}$ . On the other hand,  $f_{0,EA}$  values for devices with SnO<sub>2</sub> are larger than both  $f_{0,SDP}$  and  $f_{0,C}$ , highlighting the potential role of the probe light during the EA measurement. This observation is consistent with the electronic charges photogenerated by the probe light in devices with low surface recombination contributing to the screening dynamics, increasing the value of  $f_{0,EA}$ . We find that this hypothesis is supported by the low hysteresis index detected in the  $J$ - $V$  curve characterization [16] and, importantly, also by the large values of  $V_{OC}$  for devices with large  $f_{0,EA}$  [see Fig. 7(b) and full analysis in Sec.

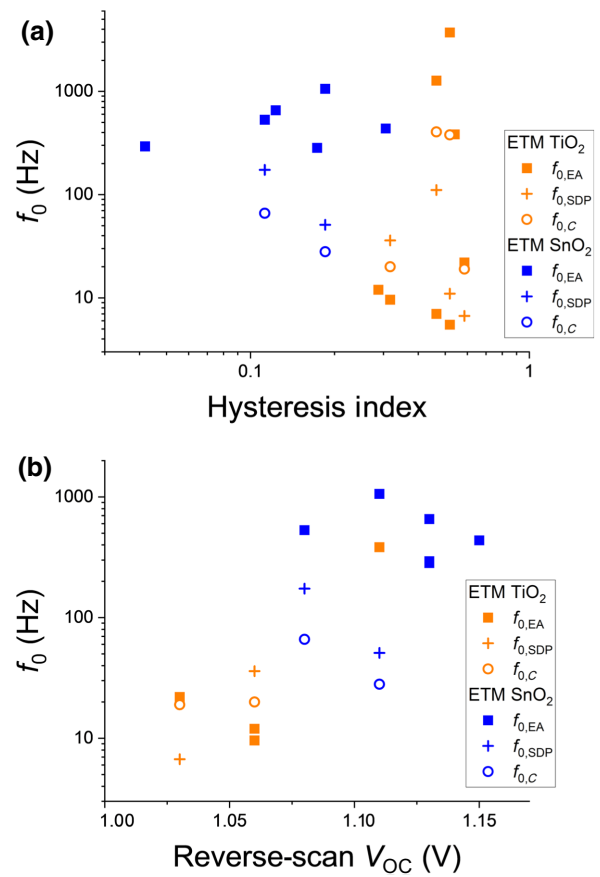


FIG. 7.  $f_0$  and photovoltaic response. Characteristic frequencies extracted from electroabsorption, step-dwell-probe, and capacitance measurements under dark conditions plotted against (a) hysteresis index, and (b)  $V_{OC}$  measured for the reverse scan (from forward bias to  $V = 0$  V) under 1-sun-equivalent illumination. For each device, values of  $f_0$  extracted with different techniques appear vertically aligned. The hysteresis index is defined from the power conversion efficiencies ( $\eta$ ) evaluated during forward and reverse scan as  $(\eta_{\text{reverse}} - \eta_{\text{forward}})/\eta_{\text{reverse}}$ . Data points referring to cells with TiO<sub>2</sub> and SnO<sub>2</sub> electron-transporting layers are shown by orange and blue markers, respectively. In (b), only devices with “bromide-poor” compositions [ $APbI_3$  and  $APb(I_{0.83}Br_{0.17})_3$ ] are considered.

10 of the Supplemental Material [41]). The correlation between  $V_{OC}$  and screening dynamics is also there when considering the trend of  $f_{0,SDP}$ , while it is less clear for  $f_{0,C}$ . Note that only devices based on perovskite compositions with comparable values of the band gap are considered in Fig. 7(b) (from the EA spectra, we expect differences in band gap  $< 50$  meV between these active layers, assuming similar exciton-binding energies).

To summarize this section, we find that active-layer compositions and device architectures showing fast screening dynamics correlate, as expected, with a low degree of hysteresis (at slow enough scan rates), and show large values of open-circuit voltage. While devices with

negligible ion transport (and therefore, with  $f_0 \rightarrow 0$  Hz) are commonly considered desirable for photovoltaic applications, our results point to electric field screening as a potentially key feature, enabling the high performance of hybrid perovskite solar cells.

## V. CONCLUSIONS

In this work, we developed frequency-dependent and time-domain transient electroabsorption spectroscopy techniques that can be applied to solar-cell devices to probe their internal electric field dynamics. By varying the frequency of the applied potential, we investigate the timescale of electric field screening for different solar-cell architectures and test the effects of experimentally accessible parameters on the internal electrostatics of the device. We compare the results with data from other techniques, such as optoelectronic transient step-dwell-probe and impedance spectroscopy, to extract independent (although indirect) evaluations of the electric field screening dynamics in devices. This set of techniques provides a number of characteristic frequencies ( $f_0$ ) that define the transition in behavior from the high-frequency electronic and dielectric response of the hybrid perovskite to a low-frequency response, where a change in applied electric field becomes screened in the perovskite. For dark conditions, we ascribe the latter to ionic defect transport and redistribution in the active layer. Under light, we find that, in addition to the process occurring at long timescales, a faster process is responsible for part of the screening. The process can be attributed to screening by a photogenerated electronic charge or to a photoenhanced ionic conductivity effect. Our analysis shows the potential of using time-resolved and frequency-domain electroabsorption to evaluate the internal electric field dynamics in hybrid perovskite solar cells and to validate the interpretation of data obtained using other optoelectronic and electrochemical techniques.

## ACKNOWLEDGMENTS

We thank Jiachen Gu and James Bannock for their help in testing the electroabsorption setup and assistance in the lab. We acknowledge funding from the UK Engineering and Physical Sciences Research Council (Grants No. EP/M025020/1, No. EP/R020574/1, No. EP/T028513/1, No. EP/R023581/1, and No. EP/M014797/1). D.M. is grateful to the Alexander von Humboldt foundation for funding. We would also like to thank Emilio Palomares for lending the expertise of his student to work on this project.

## APPENDIX A: DEVICE FABRICATION

### 1. Perovskite precursor solutions

MAPI: stoichiometric amounts of  $\text{PbI}_2$  (576 mg, 1.25 mmol, TCI Co., Ltd.) and methylammonium iodide

(MAI, 199 mg, 1.25 mmol, Greatcell Solar) are dissolved in 1 ml of a 4:1 (v:v) solvent mixture of dimethylformamide (DMF, anhydrous, Sigma-Aldrich) and dimethyl sulfoxide (DMSO, anhydrous, Sigma-Aldrich) by heating to 100 °C in a closed vial. This about 1.25M MAPI precursor solution is diluted in appropriate amounts of the DMF-DMSO solvent mixture to obtain about 0.75 and 0.625M MAPI solutions. All solutions are filtered through a 0.45- $\mu\text{m}$  syringe filter before use. According to SEM cross sections, MAPI solutions with concentrations of 1.25, 0.75, and 0.625M result in average perovskite film thicknesses of 367, 150, and 106 nm, respectively.

MAPbBrI: methylammonium bromide (MABr, Greatcell Solar, 56 mg, 0.25 mmol), MAI (119 mg, 1 mmol), and  $\text{PbI}_2$  (576 mg, 1.25 mmol) are dissolved in 1 ml DMF-DMSO (4:1, v:v) at 100 °C to obtain the nominal composition of  $\text{MAPb}(\text{Br}_{0.2}\text{I}_{0.8})_3$  in the mixed-halide perovskite precursor solution.

MAPbBr: MABr (140 mg, 1.25 mmol) and  $\text{PbBr}_2$  (TCI Co., Ltd., 459 mg, 1.25 mmol) are dissolved in 1 ml DMF-DMSO (4:1, v:v) at 100 °C.

FAMAPI: formamidinium iodide (FAI, 183 mg, 1.06 mmol), MAI (30 mg, 0.19 mmol), and  $\text{PbI}_2$  (576 mg, 1.25 mmol) are dissolved in 1 ml DMF:DMSO (4:1, v:v) at 100 °C to obtain the nominal composition of  $\text{FA}_{0.85}\text{MA}_{0.15}\text{PbI}_3$ .

FAMA: following the protocol reported by Saliba *et al.* [60], a multiple-cation mixed-halide perovskite solution is prepared by dissolving  $\text{PbI}_2$  (508 mg, 1.1 mmol),  $\text{PbBr}_2$  (80.7 mg, 0.22 mmol), FAI (171.97 mg, 1 mmol), and MABr (22.4 mg, 0.2 mmol) in 1 ml of a 4:1 (v:v) mixture of anhydrous DMF and DMSO. This nonstoichiometric precursor solution for  $(\text{FA}_{0.83}\text{MA}_{0.17}\text{Pb}(\text{I}_{0.83}\text{Br}_{0.17}))_3$  contains a 10 mol% excess of both  $\text{PbI}_2$  and  $\text{PbBr}_2$ , which is introduced to enhance the device performance. The FAMA solution is filtered through a 0.45- $\mu\text{m}$  syringe filter before use. We would like to note that volume changes upon dissolving the salts are expected.

FAMAC: CsI (389.7 mg, 1.5 mmol) is dissolved in 1 ml DMSO and filtered through a 0.45- $\mu\text{m}$  syringe filter. To obtain the desired triple-cation perovskite composition of about 5% Cs, 42  $\mu\text{l}$  of the about 1.5M CsI stock solution is added to 1 ml FAMA solution, yielding a nominal composition of  $\text{Cs}_{0.05}[(\text{FA}_{0.83}\text{MA}_{0.17})]_{0.95}\text{Pb}(\text{I}_{0.83}\text{Br}_{0.17})_3$ . The change in the I : Br ratio is neglected, and we note that volume changes upon dissolving CsI in DMSO are not taken into consideration.

FAMAR: RbI (318.5 mg, 1.5 mmol) is dissolved in 1 ml of a 4:1 (v:v) DMF-DMSO mixture and filtered through a 0.45- $\mu\text{m}$  syringe filter. To obtain the desired triple-cation perovskite composition of about 5% Rb, 42  $\mu\text{l}$  of the about 1.5M RbI stock solution is added to 1 ml of FAMA solution, yielding a nominal composition of  $\text{Rb}_{0.05}[(\text{FA}_{0.83}\text{MA}_{0.17})]_{0.95}\text{Pb}(\text{I}_{0.83}\text{Br}_{0.17})_3$ . However, it is likely that Rb is effectively not (fully) incorporated into

the perovskite structure. The change in the I : Br ratio is neglected, and we note that volume changes upon dissolving RbI in the DMF-DMSO mixture are not taken into consideration.

**FAMARC:** To obtain the quadruple-cation perovskite composition of about 5% Rb and about 5% Cs, 42  $\mu\text{l}$  of the RbI solution and 42  $\mu\text{l}$  of the CsI solution are added to 1 ml of FAMA solution, yielding a nominal composition of  $\text{Rb}_{0.05}\text{Cs}_{0.05}[(\text{FA}_{0.83}\text{MA}_{0.17})_{0.9}\text{Pb}(\text{I}_{0.83}\text{Br}_{0.17})_3]$ . The change in the I : Br ratio is neglected, and we note that volume changes upon dissolving the Cs and Rb salts are not taken into consideration to calculate the additive concentration.

## 2. Perovskite film deposition

For the MAPI, MAPbBrI, and MAPbBr films, 75  $\mu\text{l}$  of the perovskite precursor solution is spin-coated inside a nitrogen-filled glovebox at 1000 and 5000 rpm for 10 and 30 s, respectively. Approximately 15 s before the end of spinning, 500  $\mu\text{l}$  of chlorobenzene are added to the film. The MAPI films are first annealed at 40 °C for 40 min and subsequently annealed at 100 °C for 10 min. The MAPbBrI and MAPbBr films are annealed at 100 °C for 10 min. For the FAMA, FAMAC, FAMAR, and FAMARC films, the perovskite solution is spin-coated at 1000 and 4000 rpm for 10 and 30 s, respectively. Chlorobenzene is added as an antisolvent 20 s before the end of spinning. Perovskite film formation is completed by annealing at 100 °C for 60 min on a hotplate under a nitrogen atmosphere.

## 3. Device fabrication

FTO-coated glass substrates (7  $\Omega/\text{sq}$ ) are patterned by etching with zinc powder and 3M HCl solution and successively cleaned with deionized water, 2% Hellmanex detergent solution, ethanol, and finally treated with oxygen plasma for 5 min. A compact  $\text{TiO}_2$  layer is deposited as a hole-blocking layer on the substrate via a sol-gel approach. A mixture of 2M HCl (35  $\mu\text{l}$ ) and anhydrous isopropanol (2.53 ml) is added dropwise to a solution of 370- $\mu\text{l}$  titanium(IV) isopropoxide (Sigma-Aldrich) in isopropanol (2.53 ml) under vigorous stirring. The  $\text{TiO}_x$  solution is spin-coated dynamically onto the FTO substrates at 2000 rpm for 45 s, followed by annealing in air at 150 °C for 10 min and subsequently at 500 °C for 45 min. Alternatively, 10–15-nm compact  $\text{SnO}_x$  electron-transport layers are prepared by atomic layer deposition (ALD) on FTO-coated glass substrates, which are patterned and cleaned as in the  $\text{TiO}_2$  preparation. Tetrakis(dimethylaminotin)(IV) (TDMASn, Strem, 99.99%) is used as a tin precursor. Deposition is conducted at 118 °C with a base pressure of 5 mbar in a Picosun R-200 Advanced ALD reactor. The tin precursor is held at 75 °C during deposition. Ozone gas is produced by an ozone generator (INUSA AC2025). Nitrogen (99.999%, Air Liquide) is used as the

carrier and purge gas with a flow rate of 50 sccm per precursor line. The growth rate is determined via spectroscopic ellipsometry on Si(100) witness substrates. A Cauchy model is used for the tin-oxide layer and the growth rate is 0.69 Å per cycle. After deposition of the electron-transporting layer and the perovskite layer, a spiro-OMeTAD hole-transporter layer is applied. 1 ml of a solution of spiro-OMeTAD (Borun Chemicals, 99.8%) in anhydrous chlorobenzene (75 mg/ml) is doped with 10  $\mu\text{l}$  of 4-*tert*-butylpyridine (Sigma-Aldrich, 96%) and 30  $\mu\text{l}$  of a 170 mg/ml lithium bis(trifluoromethane)sulfonimide (Li-TFSI) (Sigma-Aldrich, 99.95%) solution in acetonitrile (Sigma-Aldrich, anhydrous) and deposited by spin-coating at 1500 rpm for 40 s and then 2000 rpm for 5 s. After storing the samples overnight in air at 25% relative humidity, 40-nm Au is deposited through a patterned shadow mask by thermal evaporation at  $8 \times 10^{-7}$  mbar to form the back electrode.

## APPENDIX B: DRIFT-DIFFUSION SIMULATIONS

### 1. Software

We perform drift-diffusion simulations of perovskite solar cells using the open-source software Driftfusion. The code uses MATLAB's partial differential equation solver for parabolic and elliptic equations (PDEPE) to solve the continuity equations and Poisson's equation for electron and hole densities ( $n$ ,  $p$ ), a positively charged mobile ionic charge density ( $c$ ), and the electrostatic potential ( $V$ ) as a function of position  $x$  and time  $t$ . While the software can also simulate the case with two ions, here, we focus on the case where only cations are mobile. More details on the software are available in Refs. [16,18,44]. The input parameters for the simulations are selected based on the literature and varied to obtain a similar response to the experimental observations. We use electron- and hole-transporting contacts with energy levels and work functions that are representative of the materials ( $\text{TiO}_2$ , spiro-OMeTAD). The complete parameter set used in the simulations (see also Table I), the code, and the list of commands to run the simulations are available from Ref. [61].

### 2. Impedance and electroabsorption simulations

For simulations of impedance and electroabsorption, a sinusoidal perturbation of the form

$$V_{\text{app}} = \bar{V} + \tilde{V} = \bar{V} + \Delta V \sin(\omega t) \quad (\text{B1})$$

is applied to the device stack ( $\omega = 2\pi \times \text{frequency}$ ). For impedance simulations, a small voltage amplitude is used ( $\Delta V_{\text{sim}} = 20$  mV) to match the experimental conditions ( $\Delta V_{\text{expt.}} = 20$  mV). The small signal perturbation is superimposed on a dc applied voltage,  $\bar{V} = V_{\text{OC}}$ .



TABLE I. Drift-diffusion simulation parameters. These parameters are used for simulated data, unless stated otherwise.

| Parameter   | Symbol           | HTM                    | Active layer            | ETM                    |
|---|------------------|------------------------|-------------------------|------------------------|
| Layer thickness (nm)  | $d$              | 200                    | 360                     | 200                    |
| Band gap (eV)   | $E_g$            | 2.7                    | 1.6                     | 3.2                    |
| Built-in voltage (V)  | $V_{BI}$         | 0.7                    | 0.7                     | 0.7                    |
| Relative dielectric constant  | $\epsilon_s$     | 4                      | 32                      | 30                     |
| Mobile ionic defect density (cm <sup>-3</sup> )                                 | $N_{ion}$        | 0                      | 10 <sup>19</sup>        | 0                      |
| Ion mobility (cm <sup>2</sup> V <sup>-1</sup> s <sup>-1</sup> )                 | $\mu_c$          | ...                    | 10 <sup>-10</sup>       | ...                    |
| Electron mobility (cm <sup>2</sup> V <sup>-1</sup> s <sup>-1</sup> )            | $\mu_e$          | 0.02                   | 20                      | 0.1                    |
| Hole mobility (cm <sup>2</sup> V <sup>-1</sup> s <sup>-1</sup> )                | $\mu_h$          | 0.02                   | 20                      | 0.1                    |
| Acceptor doping density (cm <sup>-3</sup> )                                     | $N_A$            | 5.8 × 10 <sup>19</sup> | ...                     | ...                    |
| Donor doping density (cm <sup>-3</sup> )  | $N_D$            | ...                    | ...                     | 5.8 × 10 <sup>19</sup> |
| Work function (eV)  | $\phi_W$         | -4.85                  | -4.6                    | -4.15                  |
| Ionization potential (eV)   | IP               | -4.9                   | -5.4                    | -7.3                   |
| Electron affinity (eV)  | $E_{aff}$        | -2.2                   | -3.8                    | -4.1                   |
| Effective density of states (cm <sup>-3</sup> )                                 | $N_c, N_V$       | 4 × 10 <sup>20</sup>   | 10 <sup>19</sup>        | 4 × 10 <sup>20</sup>   |
| Band-to-band recombination-rate coefficient (cm <sup>-3</sup> s <sup>-1</sup> ) | $k_{BTB}$        | 10 <sup>-12</sup>      | 10 <sup>-12</sup>       | 10 <sup>-12</sup>      |
| Shockley-Read-Hall trap energy (eV)   | $E_t$            | $E_{VB} + 0.15$        | $E_{CB} - 0.8$          | $E_{CB} - 0.15$        |
| Shockley-Read-Hall time constants (s)   | $\tau_n, \tau_p$ | 10 <sup>-9</sup>       | ...                     | 10 <sup>-12</sup>      |
| Generation rate (cm <sup>-3</sup> s <sup>-1</sup> )                             | $G$              | ...                    | 2.64 × 10 <sup>21</sup> | ...                    |

The open-circuit voltage is obtained for each light intensity by equilibrating the simulated device under light until it reaches the steady state. For the frequency-dependent electroabsorption simulations, the same ac and dc applied voltage amplitudes are used as in the practical experiment ( $\Delta V_{sim} = \Delta V_{expt.} = 800$  mV,  $\bar{V} = 0$  V). In every case, the number of simulated periods is extended until no variations on a larger-than-one-period scale can be observed. For the *impedance* simulations, the in-phase and out-of-phase currents are evaluated via demodulation, as previously described [18], to determine the simulated real and imaginary parts of the impedance (implemented in Analysis/IS\_EA\_ana\_demodulation.m). For *electroabsorption* measurements, the same procedure is used to evaluate the electric field in the active layer of the device, the square of which is related to changes in the absorption of the device detected via the second-harmonic electroabsorption measurements, according to Eq. (2) in the main text. The resulting real and imaginary parts of the electric field are functions of the position in the perovskite layer such that, at a given frequency, the electric field distribution in the perovskite can be expressed as (see also Sec. S2 of the Supplemental Material [41] and Sec. II):

$$\begin{aligned}
 F_{sim}(x, t) &= \bar{F}_{sim}(x) + \tilde{F}_{sim}(x, t), \\
 &= \bar{F}_{sim}(x) + \sum_{n=1}^{\infty} \Delta F_{sim, n f}(x) \\
 &\quad \times \sin[2\pi n f t + \phi_{sim, n f}(x)]. \quad (B2)
 \end{aligned}$$

We express the square of the change in electric field averaged across the perovskite film's thickness as  $F_{ms}(t)$

(implemented using Analysis/EA\_ana\_plot.m):

$$\begin{aligned}
 F_{ms}(t) &= \frac{1}{d} \int_0^d \left( \sum_{n=1}^{\infty} \Delta F_{sim, n f}(x) \sin[2\pi n f t + \phi_{sim, n f}(x)] \right)^2 \\
 &\quad \times dx, \quad (B3)
 \end{aligned}$$

where  $d$  is the thickness of the perovskite layer. By extracting the second-harmonic component,  $F_{ms}|_{2f}(t)$ , from  $F_{ms}(t)$ , one obtains

$$F_{ms}|_{2f}(t) = (\Delta F_{sim})^2 \sin(2\pi 2f t + \phi_{sim, 2f}) \quad (B4)$$

The amplitude,  $(\Delta F_{sim})^2$ , of this harmonic is the quantity of interest, in that  $\Delta T_{2f}/\bar{T} \propto (\Delta F_{sim})^2$ .  $\Delta F_{sim}$  is used in this work as a quantity that can be compared with the experimental EA signal,  $(\Delta T_{2f}/\bar{T})^{1/2}$ .

### 3. Step-dwell-probe simulations

Simulations of step-dwell-probe measurements are performed by following a perturbation protocol consistent with the experimental procedure:

- (a) The device is equilibrated in the dark at short circuit.
- (b) At  $t=0$  s, a forward-bias voltage step of 0.6 V is applied to the stack. For SDP under light, a bias light is simultaneously included at this point.
- (c) The device is kept at 0.6 V for a variable dwell time  $\Delta t$ .
- (d) A monochromatic light pulse (wavelength 638 nm) with an intensity of 1-sun equivalent (the light intensity is estimated by matching the short-circuit current obtained at 1-sun AM1.5) is applied. The pulse duration is long

enough to resolve the electronic photocurrent value after the initial transient, similarly to the experiment. The time after the beginning of the pulse at which the current is recorded is referred to as the sampling time.

(e) From the resulting transient photocurrent (function of  $\Delta t$ ), the value of  $\Delta J_{\text{sim}}$  is extracted as the final value during application of the pulse.

### APPENDIX C: FIRST-HARMONIC ELECTROABSORPTION

Figure 8 shows first-harmonic EA measurements run on the reference MAPI solar-cell structure for different values of the ac voltage amplitude,  $\Delta V$ . The scaling of the spectra magnitude does not follow the expected linear dependence, with some clear changes in spectral shape. For MAPI cells, we find that the shape and magnitude of the first-harmonic spectrum under nominally identical conditions can vary, depending on the history of the sample, despite stabilization times before measurements over 200 s. This can be ascribed to changes in the static electric field,  $\bar{V}$ , which this signal depends on [see Eq. (1)], but also to other possible induced changes in absorbance.

Figures 9(a) and 10(a) show first-harmonic EA measurements on MAPI and MAPbBr<sub>3</sub> solar cells, respectively. The shape of the first- and second-harmonic spectra are compared under the same perturbation ( $\bar{V} = 0$  V and  $\Delta V = 0.5$  V at 1 kHz). Figures 9(b) and 10(b) display first-harmonic transient EA measurements under similar conditions used to collect data shown in Fig. 5, including both increasing and decreasing voltage-step experiments ( $\bar{V} = 0$  V  $\rightarrow$  0.5 V step and for a  $\bar{V} = 0.5$  V  $\rightarrow$  0 V).

### APPENDIX D: dc-VOLTAGE-DEPENDENT ELECTROABSORPTION

When varying the value of  $\bar{V}$ , we observe changes in magnitude and slight changes in shape for the

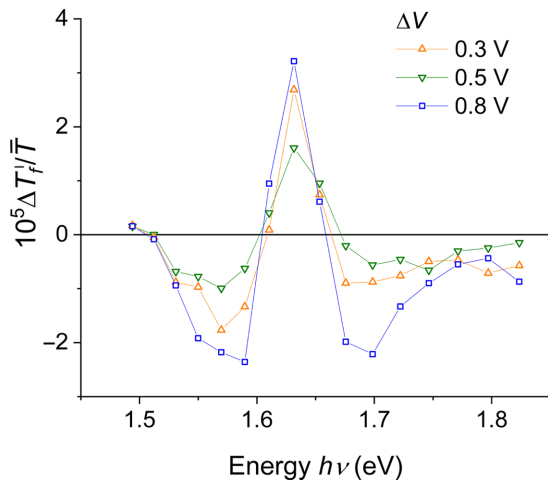


FIG. 8. First-harmonic electroabsorption measurements on a TiO<sub>2</sub>/MAPI/spiro-OMeTAD device. Measurements are performed using  $\bar{V} = 0$  V and different values of  $\Delta V$  at 1 kHz.

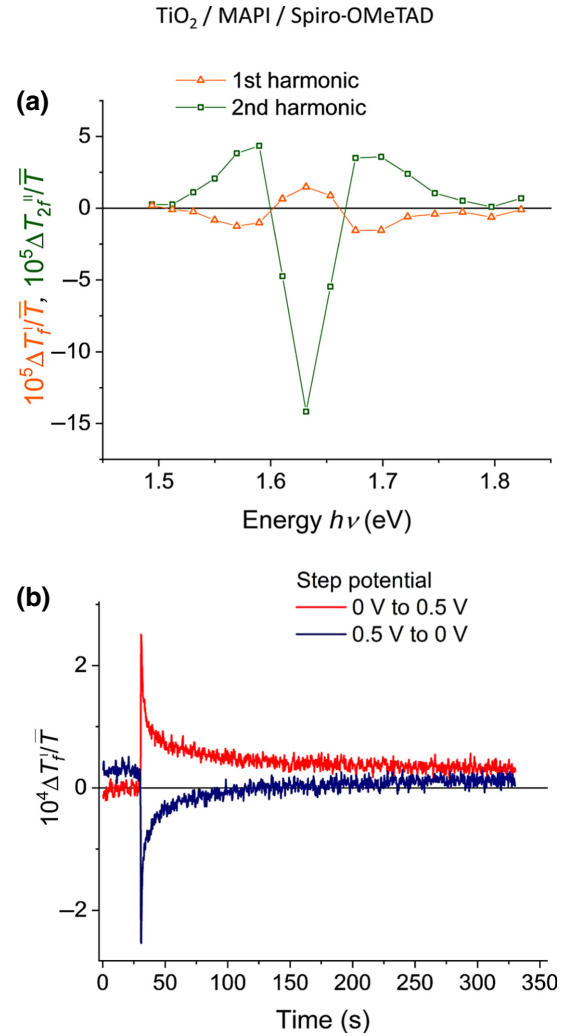


FIG. 9. First-harmonic electroabsorption measurements on a TiO<sub>2</sub>/MAPI/spiro-OMeTAD device. (a) Comparison between first- and second-harmonic signals. (b) Transient electroabsorption of the first-harmonic signal for a  $\bar{V} = 0$  V  $\rightarrow$  0.5 V step and for a  $\bar{V} = 0.5$  V  $\rightarrow$  0 V step probed at 760 nm.

second-harmonic EA spectrum (Fig. 11). The trend is consistent with transient data shown in Fig. 5(b), whereby the application of a forward bias results in a larger signal magnitude compared with the  $\bar{V} = 0$  V case.

Figure 12 shows the changes in the second-harmonic EA signal at 760 nm of a MAPI solar cell while scanning the value of  $\bar{V}$ . Different voltage scan rates are reflected in slightly different hystereses in the data. This can be correlated to hysteresis in the electric field in the cell.

Figure 13 highlights a small change in the screening dynamics observed when measuring the frequency-dependent second-harmonic EA signal at 760 nm while applying  $\bar{V} = 0$  or 0.5 V.

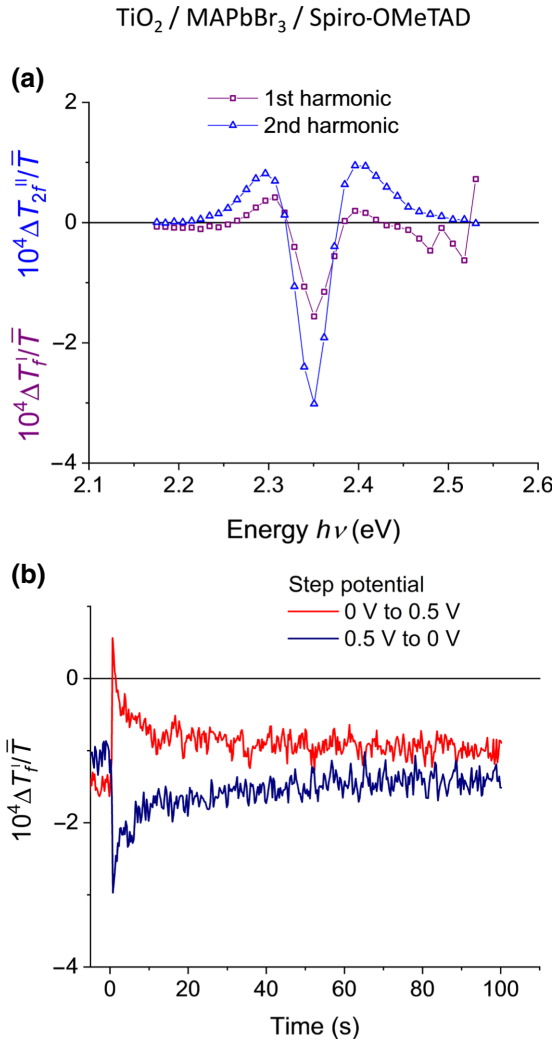


FIG. 10. First-harmonic electroabsorption measurements on a  $\text{TiO}_2/\text{MAPbBr}_3/\text{spiro-OMeTAD}$  device. (a) Comparison between first- and second-harmonic signals. (b) Transient electroabsorption of the first-harmonic signal for a  $\bar{V} = 0 \text{ V} \rightarrow 0.5 \text{ V}$  step and for a  $\bar{V} = 0.5 \text{ V} \rightarrow 0 \text{ V}$  step probed at 527.5 nm.

#### APPENDIX E: EA STUDY ON DIFFERENT HALIDE AND *A*-CATION COMPOSITIONS

We perform frequency-dependent second-harmonic EA measurements on solar-cell devices with active layers of different compositions. Figure 14 shows the results for bromide and mixed iodide-bromide perovskites. Data are shown for the dark situation (probe light still present) and for situations where a white-LED bias light is used. For  $\text{MAPbBr}_3$ , we find that screening seems to occur over two different timescales, with a first decrease in signal magnitude around 1 kHz and a sharper drop occurring below 10 Hz.

Application of the bias light results in an overall reduction in magnitude, while no clear change in frequency dependence is detected. We observe similar behavior for the  $\text{MAPI}_{0.8}\text{Br}_{0.2}$  solar cell in the dark. Under light, this

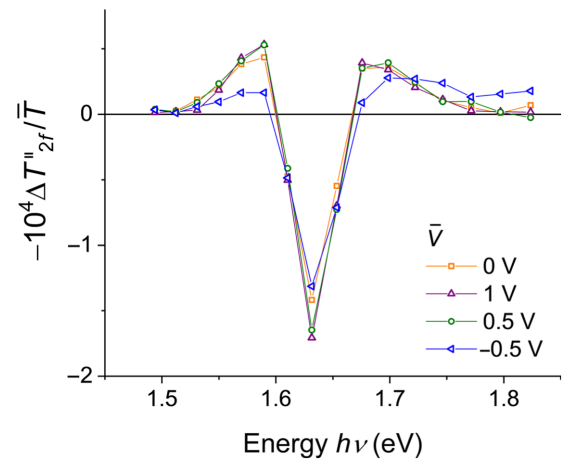


FIG. 11.  $\bar{V}$  dependence of the second-harmonic EA performed on a  $\text{TiO}_2/\text{MAPI}/\text{spiro-OMeTAD}$  device. Measurements are performed using  $\Delta V = 0.5 \text{ V}$  at 1 kHz. Before each measurement, the cell is left to equilibrate for  $>200 \text{ s}$  at each value of  $\bar{V}$ .

device shows a more complex response, which could be related to the presence of two halide ions.

We also investigate solar cells with mixed-cation mixed-halide compositions  $A\text{Pb}(\text{I}_{0.83}\text{Br}_{0.17})_3$ . The *A*-cation composition is changed while keeping the same halide ratio. The results, shown in Fig. 15, indicate that faster screening occurs for these active layers compared to MAPI. At frequencies  $>1 \text{ kHz}$ , we observe different behavior for the solar cell containing rubidium but no cesium cations.

Figure 16 shows that  $f_{0,EA}$  in the order of 1 kHz is obtained for a  $\text{Cs}_{0.05}[(\text{FA}_{0.83}\text{MA}_{0.17})_{0.95}\text{Pb}(\text{I}_{0.83}\text{Br}_{0.17})_3]$  solar cell, whether  $\text{TiO}_2$  or  $\text{SnO}_2$  is used as the electron-transport material.

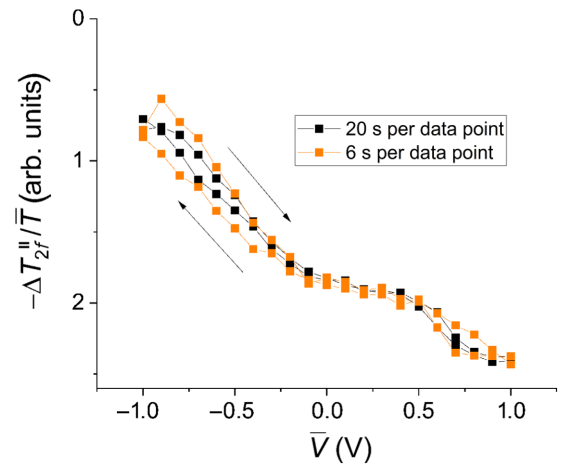


FIG. 12.  $\bar{V}$  dependence of the second-harmonic electroabsorption signal at 760 nm of a  $\text{TiO}_2/\text{MAPI}/\text{spiro-OMeTAD}$  device. Lock-in time constant is set at 0.3 s for the orange data set and at 1 s for the black data set. In both cases, the perturbation frequency is 1 kHz with a voltage amplitude of 0.5 V. At each voltage step, the measurement takes 6 and 20 s before moving to the next data point.

### APPENDIX F: ANALYTICAL EXPRESSIONS FOR $f_0$

Based on the circuit model in Fig. 2(e), it is possible to extract an analytical expression for the values of the  $f_0$  parameters used in this study:

(a)  $f_{0,EA}$ : this can be associated to the pole in the expression of the transfer function relating the potential dropping in the series  $C_B, R_{ion}, C_C$  and the applied potential.

(b)  $f_{0,C}$ : this is extracted from the intersection of the capacitance at high frequencies ( $C_{bulk,per}$ ) and the low-frequency capacitance behavior.

For simplicity, we consider the case of  $C_A = C_D = C_{con}$  and  $C_B = C_C = C_{per}$ . The transfer function,  $G_{EA}(\omega)$ , relating the change in potential dropping across the perovskite layer,  $\tilde{V}_{per}$ , and the applied voltage,  $\tilde{V}$ , can be expressed as follows:

$$G_{EA}(\omega) = \frac{\tilde{V}_{per}(\omega)}{\tilde{V}} = \frac{C_{con}}{C_{con} + C_{per}} \frac{1 + i\omega R_{ion}((C_{per}/2) + C_{bulk,per})}{1 + i\omega R_{ion}((1/2)[C_{per}C_{con}/(C_{con} + C_{per})] + C_{bulk,per})}. \quad (F1)$$

From Eq. (F1), we note the following:

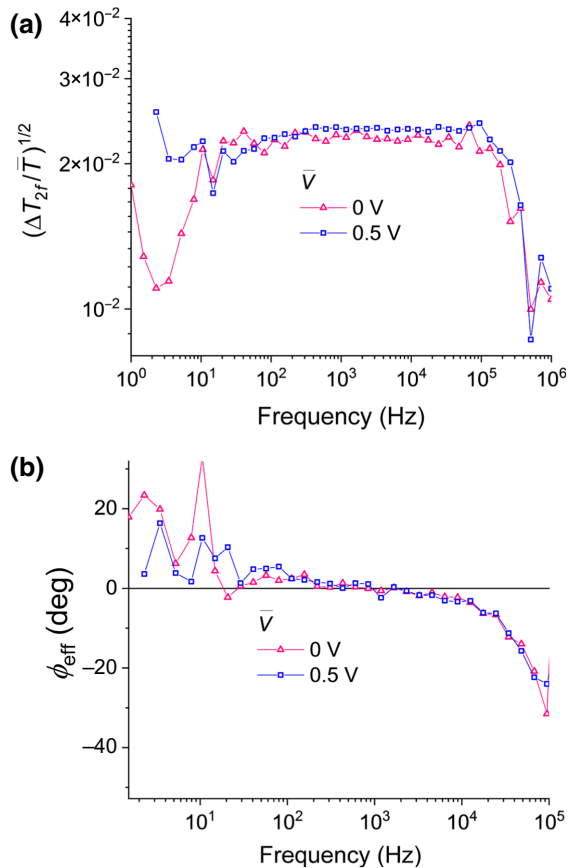


FIG. 13.  $\bar{V}$  dependence of second-harmonic frequency-dependent EA. Frequency-dependent (a) magnitude and (b) phase of the second-harmonic electroabsorption for a  $\text{TiO}_2/\text{MAPI}/\text{spiro-OMeTAD}$  solar cell using different values of dc voltage.

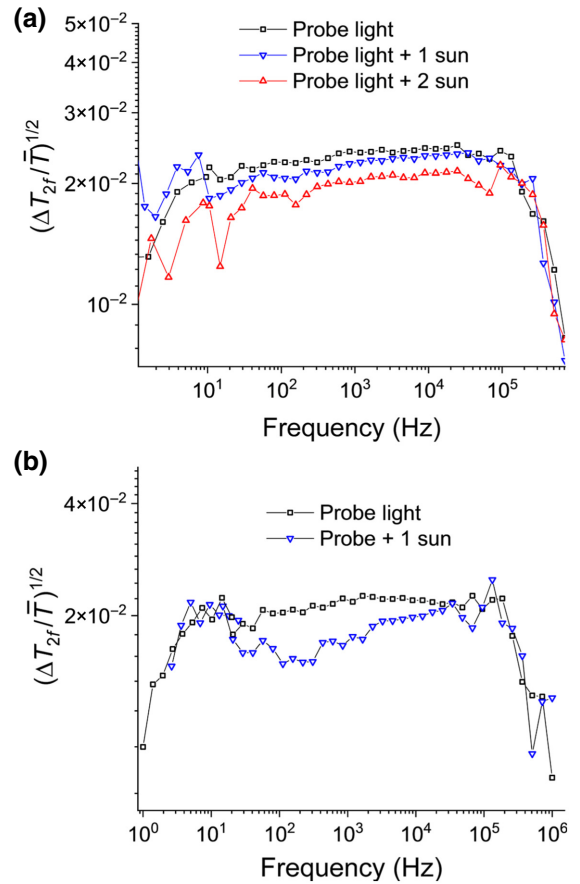


FIG. 14. Frequency-dependent second-harmonic electroabsorption on  $\text{MAPbBr}_3$  and  $\text{MAPI}_{0.8}\text{Br}_{0.2}$  devices. Different bias-light-intensity conditions are considered. (a)  $\text{TiO}_2/\text{MAPbBr}_3/\text{spiro-OMeTAD}$ ; (b)  $\text{TiO}_2/\text{MAPI}_{0.8}\text{Br}_{0.2}/\text{spiro-OMeTAD}$ .

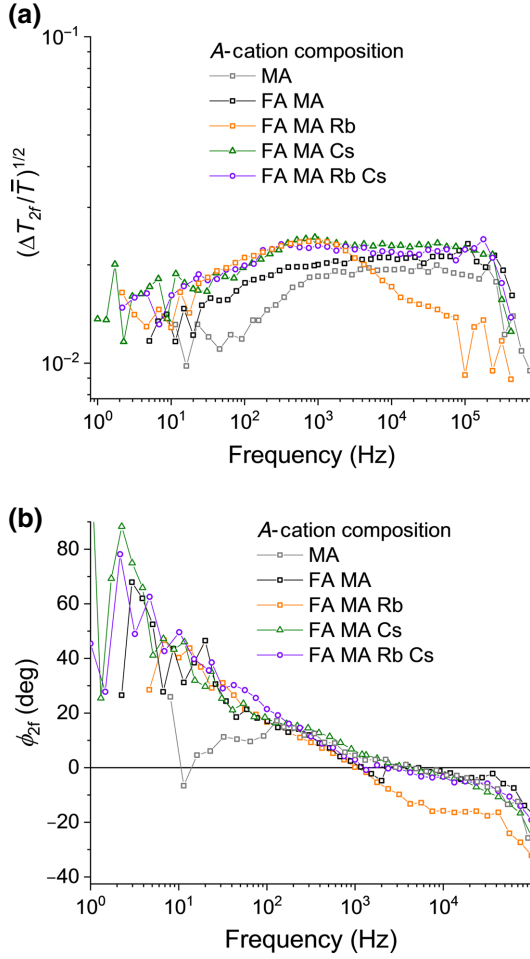


FIG. 15. Frequency-dependent EA measurements on solar cells with different  $A$ -cation compositions. (a) Square-root of the magnitude and (b) effective phase of the 2<sup>nd</sup> harmonic frequency-dependent electroabsorption of  $\text{SnO}_2/\text{APb}(\text{I}_{0.83}\text{Br}_{0.17})_3/\text{spiro-OMeTAD}$  solar cells, where different  $A$ -cation compositions are tested. Solar cell with MA-only  $A$  cation is a MAPI-based device. For details regarding the composition, see Appendix A.

(a)  $G_{\text{EA}}(\omega \rightarrow 0) \rightarrow C_{\text{con}}/(C_{\text{con}} + C_{\text{per}})$ , which is a constant real value, and therefore, has a phase of  $0^\circ$ .

(b) For large values of  $C_{\text{per}}$ ,

$$G_{\text{EA}}(\omega) \approx \frac{i\omega R_{\text{ion}}(C_{\text{con}}/2)}{1 + i\omega R_{\text{ion}}((C_{\text{con}}/2) + C_{\text{bulk,per}})}, \quad (\text{F2})$$

and, in such a case,  $G_{\text{EA}}(\omega \rightarrow 0) \approx i\omega R_{\text{ion}}(C_{\text{con}}/2)$  (phase  $90^\circ$ ). We also identify  $f_{0,\text{EA}}$  as

$$f_{0,\text{EA}} = \frac{1}{2\pi R_{\text{ion}}((1/2)[C_{\text{per}}C_{\text{con}}/(C_{\text{con}} + C_{\text{per}})] + C_{\text{bulk,per}})}. \quad (\text{F3})$$

For  $C_{g,\text{per}} \ll C_{\text{con}}$  and  $C_{g,\text{per}} \ll C_{\text{per}}$ ,

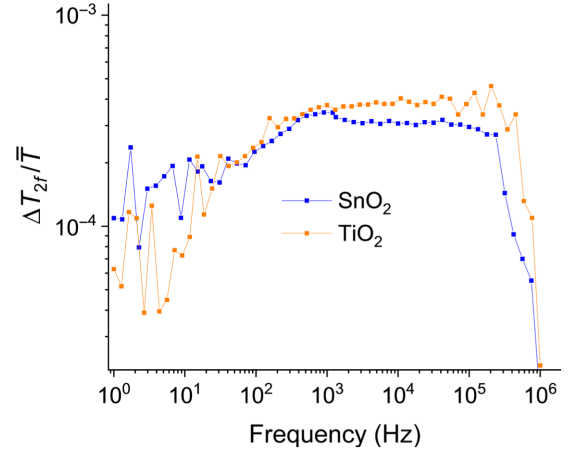


FIG. 16. ETL dependence of EA measurements on triple-cation solar cells. Frequency-dependent second-harmonic EA of  $\text{Cs}_{0.05}[(\text{FA}_{0.83}\text{MA}_{0.17})_{0.95}\text{Pb}(\text{I}_{0.83}\text{Br}_{0.17})_3/\text{spiro-OMeTAD}]$  solar cells with either  $\text{TiO}_2$  or  $\text{SnO}_2$  electron-transporting materials.

$$\begin{aligned} f_{0,\text{EA}} &= \frac{1}{2\pi R_{\text{ion}}(1/2)[C_{\text{per}}C_{\text{con}}/(C_{\text{con}} + C_{\text{per}})]} \\ &= \frac{1}{2\pi R_{\text{ion}}C_{\text{ion}}^\perp/2}. \end{aligned} \quad (\text{F4})$$

For the characteristic frequency associated with capacitance measurements,  $f_{0,C}$ ,

$$f_{0,C} = \frac{1}{2\pi R_{\text{ion}}C_{\text{ion}}^\perp/2} \sqrt{\frac{C_{\text{ion}}^\perp/2}{C_{g,\text{per}}}}. \quad (\text{F5})$$

Equation (F5) shows that  $f_{0,C}$  cannot be used to compare characteristic frequencies of different devices in a straightforward way, due to the  $\sqrt{(1/2)(C_{\text{ion}}^\perp/C_{g,\text{per}})}$  factor, which can vary, depending on the contacts and the active-layer composition and thickness. Also, note that the values of  $C_{\text{per}}$  and  $C_{\text{con}}$  are functions of the applied voltage. Here, such a dependence is not explicitly considered. While for small perturbation measurements (e.g., impedance) a constant value of capacitance can be used for any given steady-state condition, the treatment for large perturbation measurements (e.g., EA) is more complex.

The expressions above refer to the case of a cell in the dark and are extracted by considering the ionic branch of the circuit model in Fig. 2(e). Under light, the circuit model is able to explain the behavior observed from impedance, where an increase in the low-frequency apparent capacitance occurs due to ionic-to-electronic current amplification. One can also express the value of  $f_{0,C}$  analytically in that case. As noted in the main text, such a value is expected to increase with light intensity, despite the unchanging time constant of the ionic branch in the circuit model. Changes in  $C_{\text{per}}$ ,  $C_{\text{con}}$ , and  $R_{\text{ion}}$  as a function of

bias can explain the changes in  $f_{0,EA}$  observed experimentally when applying light to the solar cells investigated in this study.

- 
- [1] S. D. Stranks, G. E. Eperon, G. Grancini, C. Menelaou, M. J. P. Alcocer, T. Leijtens, L. M. Herz, A. Petrozza, and H. J. Snaith, Electron-hole diffusion lengths exceeding 1 micrometer in an organometal trihalide perovskite absorber, *Science* **342**, 341 (2013).
- [2] B. C. O'Regan, P. R. F. Barnes, X. Li, C. Law, E. Palomares, and J. M. Marin-beloqui, Optoelectronic studies of methylammonium lead iodide perovskite solar cells with mesoporous TiO<sub>2</sub>: Separation of electronic and chemical charge storage, understanding two recombination lifetimes, and the evolution of band offsets during  $J-V$  hysteresis, *J. Am. Chem. Soc.* **137**, 5087 (2015).
- [3] A. Pockett, G. E. Eperon, N. Sakai, H. J. Snaith, L. M. Peter, and P. J. Cameron, Microseconds, milliseconds and seconds: Deconvoluting the dynamic behaviour of planar perovskite solar cells, *Phys. Chem. Chem. Phys.* **19**, 5959 (2017).
- [4] H. J. Snaith, A. Abate, J. M. Ball, G. E. Eperon, T. Leijtens, N. Noel, S. D. Stranks, J. T. W. Wang, K. Wojciechowski, and W. Zhang, Anomalous hysteresis in perovskite solar cells, *J. Phys. Chem. Lett.* **5**, 1511 (2014).
- [5] I. Zarazua and J. Bisquert, Light-induced space-charge accumulation zone as photovoltaic mechanism in perovskite solar cells, *J. Phys. Chem. Lett.* **7**, 5 (2016).
- [6] T. Y. Yang, G. Gregori, N. Pellet, M. Grätzel, and J. Maier, The significance of ion conduction in a hybrid organic-inorganic lead-iodide-based perovskite photosensitizer, *Angew. Chem., Int. Ed.* **54**, 7905 (2015).
- [7] C. Eames, J. M. Frost, P. R. F. Barnes, B. C. O'Regan, A. Walsh, and M. S. Islam, Ionic transport in hybrid lead iodide perovskite solar cells, *Nat. Commun.* **6**, 2 (2015).
- [8] D. Moia and J. Maier, Ion transport, defect chemistry, and the device physics of hybrid perovskite solar cells, *ACS Energy Lett.* **6**, 1566 (2021).
- [9] A. Senocrate, I. Moudrakovski, G. Y. Kim, T.-Y. Yang, G. Gregori, M. Grätzel, and J. Maier, The nature of ion conduction in methylammonium lead iodide: A multimethod approach, *Angew. Chem., Int. Ed.* **56**, 7755 (2017).
- [10] Z. Xiao and J. Huang, Energy-efficient hybrid perovskite memristors and synaptic devices, *Adv. Electron. Mater.* **2**, 1600100 (2016).
- [11] X. Zhao, H. Xu, Z. Wang, Y. Lin, and Y. Liu, Memristors with organic-inorganic halide perovskites, *InfoMat* **1**, 183 (2019).
- [12] C. C. Boyd, R. Cheacharoen, T. Leijtens, and M. D. McGehee, Understanding degradation mechanisms and improving stability of perovskite photovoltaics, *Chem. Rev.* **119**, 3418 (2019).
- [13] A. Senocrate, G. Y. Kim, M. Grätzel, and J. Maier, Thermochemical stability of hybrid halide perovskites, *ACS Energy Lett.* **4**, 2859 (2019).
- [14] L. Zhao, R. A. Kerner, Z. Xiao, Y. L. Lin, K. M. Lee, J. Schwartz, and B. P. Rand, Redox chemistry dominates the degradation and decomposition of metal halide perovskite optoelectronic devices, *ACS Energy Lett.* **1**, 595 (2016).
- [15] S. P. Dunfield, L. Bliss, F. Zhang, J. M. Luther, K. Zhu, M. F. A. M. van Hest, M. O. Reese, and J. J. Berry, From defects to degradation: A mechanistic understanding of degradation in perovskite solar cell devices and modules, *Adv. Energy Mater.* **10**, 1904054 (2020).
- [16] P. Calado, A. M. Telford, D. Bryant, X. Li, J. Nelson, B. C. O'Regan, and P. R. F. Barnes, Evidence for ion migration in hybrid perovskite solar cells with minimal hysteresis, *Nat. Commun.* **7**, 13831 (2016).
- [17] L. Schmidt-Mende, *et al.*, Roadmap on organic-inorganic hybrid perovskite semiconductors and devices, *APL Mater.* **9**, 109202 (2021).
- [18] D. Moia, I. Gelmetti, M. Stringer, O. Game, D. Lidzey, E. Palomares, P. Calado, J. Nelson, W. Fisher, and P. R. F. Barnes, Ionic-to-electronic current amplification in hybrid perovskite solar cells: Ionically gated transistor-interface circuit model explains hysteresis and impedance of mixed conducting devices, *Energy Environ. Sci.* **12**, 1296 (2019).
- [19] V. W. Bergmann, S. A. L. Weber, F. Javier Ramos, M. K. Nazeeruddin, M. Grätzel, D. Li, A. L. Domanski, I. Lieberwirth, S. Ahmad, and R. Berger, Real-space observation of unbalanced charge distribution inside a perovskite-sensitized solar cell, *Nat. Commun.* **5**, 5001 (2014).
- [20] S. A. L. Weber, I. M. Hermes, S. H. Turren-Cruz, C. Gort, V. W. Bergmann, L. Gilson, A. Hagfeldt, M. Graetzel, W. Tress, and R. Berger, How the formation of interfacial charge causes hysteresis in perovskite solar cells, *Energy Environ. Sci.* **11**, 2404 (2018).
- [21] E. Edri, S. Kirmayer, S. Mukhopadhyay, K. Gartsman, G. Hodes, and D. Cahen, Elucidating the charge carrier separation and working mechanism of CH<sub>3</sub>NH<sub>3</sub>PbI<sub>3-x</sub>Cl<sub>x</sub> perovskite solar cells, *Nat. Commun.* **5**, 3461 (2014).
- [22] S. T. Birkhold, J. T. Pecht, R. Giridharagopal, G. E. Eperon, L. Schmidt-mende, and D. S. Ginger, Direct observation and quantitative analysis of mobile Frenkel defects in metal halide perovskites using scanning kelvin probe microscopy, *J. Phys. Chem. C* **122**, 12633 (2018).
- [23] P. Calado and P. R. F. Barnes, Ionic screening in perovskite  $p-n$  homojunctions, *Nat. Energy* **6**, 589 (2021).
- [24] V. Roiati, E. Mosconi, A. Listorti, S. Colella, G. Gigli, and F. De Angelis, Stark effect in perovskite/TiO<sub>2</sub> solar cells: Evidence of local interfacial order, *Nano Lett.* **14**, 2168 (2014).
- [25] M. E. Ziffer, J. C. Mohammed, and D. S. Ginger, Electroabsorption spectroscopy measurements of the exciton binding energy, electron-hole reduced effective mass, and band gap in the perovskite CH<sub>3</sub>NH<sub>3</sub>PbI<sub>3</sub>, *ACS Photonics* **3**, 1060 (2016).
- [26] A. A. Paraecattil, J. De Jonghe-Risse, V. Pranculis, J. Teuscher, and J. E. Moser, Dynamics of photocarrier separation in MAPbI<sub>3</sub> perovskite multigrain films under a quasistatic electric field, *J. Phys. Chem. C* **120**, 19595 (2016).
- [27] M. E. F. Bouduban, A. Burgos-Caminal, R. Ossola, J. Teuscher, and J.-E. Moser, Energy and charge transfer cascade in methylammonium lead bromide perovskite nanoparticle aggregates, *Chem. Sci.* **8**, 4371 (2017).

- [28] F. Ruf, A. Magin, M. Schultes, E. Ahlswede, H. Kalt, and M. Hetterich, Excitonic nature of optical transitions in electroabsorption spectra of perovskite solar cells, *Appl. Phys. Lett.* **112**, 083902 (2018).
- [29] K. Awasthi, K.-B. Du, C.-Y. Wang, C.-L. Tsai, M. Hamada, S. Narra, E. W. Diau, and N. Ohta, Electroabsorption studies of multicolored lead halide perovskite nanocrystalline solid films, *ACS Photonics* **5**, 2408 (2018).
- [30] M. Hamada, S. Rana, E. Jokar, K. Awasthi, E. W. G. Diau, and N. Ohta, Temperature-dependent electroabsorption spectra and exciton binding energy in a perovskite  $\text{CH}_3\text{NH}_3\text{PbI}_3$  nanocrystalline film, *ACS Appl. Energy Mater.* **3**, 11830 (2020).
- [31] K. R. Hansen, C. E. McClure, J. S. Colton, and L. Whittaker-Brooks, Franz-Keldysh and Stark Effects in Two-Dimensional Metal Halide Perovskites, *Phys. Rev. X Energy* **1**, 013001 (2022).
- [32] V. Kattoor, K. Awasthi, E. Jokar, E. W. G. Diau, and N. Ohta, Integral method analysis of electroabsorption spectra and electrophotoluminescence study of  $(\text{C}_4\text{H}_9\text{NH}_3)_2\text{PbI}_4$  organic-inorganic quantum well, *J. Phys. Chem. C* **122**, 26623 (2018).
- [33] X. Wu, H. Yu, N. Li, F. Wang, H. Xu, and N. Zhao, Composition-dependent light-induced dipole moment change in organometal halide perovskites, *J. Phys. Chem. C* **119**, 1253 (2015).
- [34] C. Li, S. Tscheuschner, F. Paulus, P. E. Hopkinson, J. Kießling, A. Köhler, Y. Vaynzof, and S. Huettner, Iodine migration and its effect on hysteresis in perovskite solar cells, *Adv. Mater.* **28**, 2446 (2016).
- [35] S. Rana, K. Awasthi, S. S. Bhosale, E. W. G. Diau, and N. Ohta, Temperature-dependent electroabsorption and electrophotoluminescence and exciton binding energy in  $\text{MAPbBr}_3$  perovskite quantum dots, *J. Phys. Chem. C* **123**, 19927 (2019).
- [36] S. Rana, K. Awasthi, E. W.-G. Diau, and N. Ohta, Illumination power-dependent electroabsorption of excitons in a  $\text{CH}_3\text{NH}_3\text{PbI}_3$  perovskite film, *J. Phys. Chem. C* **125**, 27631 (2021).
- [37] G. U. Bublitz and S. G. Boxer, Stark spectroscopy: Applications in chemistry, biology, and materials science, *Annu. Rev. Phys. Chem.* **48**, 213 (1997).
- [38] P. Y. Yu and M. Cadorna, *Fundamentals of Semiconductors*, 4th ed. (Springer-Verlag, Berlin, Heidelberg, 2010).
- [39] J. C. DeMello, J. J. M. Halls, S. C. Graham, N. Tessler, and R. H. Friend, Electric Field Distribution in Polymer Light-Emitting Electrochemical Cells, *Phys. Rev. Lett.* **85**, 421 (2000).
- [40] P. J. Brewer, A. J. deMello, and J. C. deMello, Influence of carrier injection on the electromodulation response of trap-rich polymer light-emitting diodes, *J. Appl. Phys.* **99**, 114502 (2006).
- [41] See the Supplemental Material at <http://link.aps.org/supplemental/10.1103/PhysRevApplied.18.044056> for an analysis of frequency-dependent second-harmonic electroabsorption and interpretation of electric field screening, drift-diffusion simulations, a first-harmonic electroabsorption study, step-dwell-probe measurements, a morphology study of MAPI, further electroabsorption measurements, impedance characterization, current-voltage curves of perovskite solar cells, and impedance study of contact layers, and  $f_0$  versus photovoltaic parameters.
- [42] P. R. F. Barnes, K. Miettunen, X. Li, A. Y. Anderson, T. Bessho, M. Gratzel, and B. C. O'Regan, Interpretation of optoelectronic transient and charge extraction measurements in dye-sensitized solar cells, *Adv. Mater.* **25**, 1881 (2013).
- [43] R. A. Belisle, W. H. Nguyen, A. R. Bowering, P. Calado, X. Li, S. J. C. Irvine, M. D. McGehee, P. R. F. Barnes, and B. C. O'Regan, Interpretation of inverted photocurrent transients in organic lead halide perovskite solar cells: Proof of the field screening by mobile ions and determination of the space charge layer widths, *Energy Environ. Sci.* **10**, 192 (2017).
- [44] P. Calado, I. Gelmetti, B. Hilton, M. Azzouzi, J. Nelson, and P. R. F. Barnes, Driftdiffusion: An open source code for simulating ordered semiconductor devices with mixed ionic-electronic conducting materials in one-dimension, *J. Comput. Electron.* **21**, 960 (2022).
- [45] D. E. Aspnes and J. E. Rowe, Resonant nonlinear optical susceptibility: Electroreflectance in the low-field limit, *Phys. Rev. B* **5**, 4022 (1972).
- [46] A. Frova and D. E. Aspnes, Combined investigation of nonuniform-field electroreflectance and surface galvanomagnetic properties in germanium, *Phys. Rev.* **182**, 795 (1969).
- [47] L. Bertoluzzi, R. A. Belisle, K. A. Bush, R. Cheacharoen, M. D. McGehee, and B. C. O'Regan, *In situ* measurement of electric-field screening in hysteresis-free  $\text{PTAA/FA}_{0.83}\text{Cs}_{0.17}\text{Pb}(\text{I}_{0.83}\text{Br}_{0.17})_3/\text{C}_{60}$  perovskite solar cells gives an ion mobility of  $\sim 3 \times 10^{-7} \text{ cm}^2/(\text{V s})$ , 2 orders of magnitude faster than reported for metal-oxide-contacted perovskite cells with hysteresis, *J. Am. Chem. Soc.* **140**, 12775 (2018).
- [48] K. Awasthi, K. Kala, S. Rana, D. Shailesh, E. W. G. Diau, and N. Ohta, Switching between spectral broadening and narrowing of the exciton absorption band of a  $\text{CH}_3\text{NH}_3\text{PbI}_3$  film on altering the polarity of an applied electric field, *Appl. Phys. Lett.* **116**, 251101 (2020).
- [49] D. A. Jacobs, H. Shen, F. Pfeffer, J. Peng, T. P. White, F. J. Beck, R. Kylie, D. A. Jacobs, H. Shen, F. Pfeffer, *et al.*, The two faces of capacitance: New interpretations for electrical impedance measurements of perovskite solar cells and their relation to hysteresis, *J. Appl. Phys.* **124**, 225702 (2018).
- [50] A. Senocrate, I. Moudrakovski, and J. Maier, Short-range ion dynamics in methylammonium lead iodide by multinuclear solid state NMR and 127I NQR, *Phys. Chem. Chem. Phys.* **20**, 20043 (2018).
- [51] Y. Yuan and J. Huang, Ion migration in organometal trihalide perovskite and its impact on photovoltaic efficiency and stability, *Acc. Chem. Res.* **49**, 286 (2016).
- [52] D. R. Ceratti, A. Zohar, R. Kozlov, H. Dong, G. Uraltsev, O. Girshevitz, I. Pinkas, L. Avram, G. Hodes, and D. Cahen, Eppur si muove: Proton diffusion in halide perovskite single crystals, *Adv. Mater.* **32**, 2002467 (2020).
- [53] L. M. Herz, Charge-carrier mobilities in metal halide perovskites: Fundamental mechanisms and limits, *ACS Energy Lett.* **2**, 1539 (2017).

- [54] G. Y. Kim, A. Senocrate, T. Yang, G. Gregori, M. Grätzel, and J. Maier, Large tunable photoeffect on ion conduction in halide perovskites and implications for photodecomposition, *Nat. Mater.* **17**, 445 (2018).
- [55] R. A. Evarestov, E. A. Kotomin, A. Senocrate, R. K. Kremer, and J. Maier, First-principles comparative study of perfect and defective  $\text{CsPbX}_3$  ( $X = \text{Br, I}$ ) crystals, *Phys. Chem. Chem. Phys.* **22**, 3914 (2020).
- [56] G. Y. Kim, A. Senocrate, Y. R. Wang, D. Moia, and J. Maier, Photo-effect on ion transport in mixed cation and halide perovskites and implications for photo-demixing, *Angew. Chem., Int. Ed.* **60**, 820 (2021).
- [57] A. Senocrate, I. Moudrakovski, T. Acartürk, R. Merkle, G. Y. Kim, U. Starke, M. Grätzel, and J. Maier, Slow  $\text{CH}_3\text{NH}_3^+$  diffusion in  $\text{CH}_3\text{NH}_3\text{PbI}_3$  under light measured by solid-state NMR and tracer diffusion, *J. Phys. Chem. C* **122**, 21803 (2018).
- [58] G. Y. Kim, A. Senocrate, D. Moia, and J. Maier, Ionically generated built-in equilibrium space charge zones—a paradigm change for lead halide perovskite interfaces, *Adv. Funct. Mater.* **30**, 2002426 (2020).
- [59] S. N. Habisreutinger, N. K. Noel, and H. J. Snaith, Hysteresis index: A figure without merit for quantifying hysteresis in perovskite solar cells, *ACS Energy Lett.* **3**, 2472 (2018).
- [60] M. Saliba, T. Matsui, K. Domanski, J. Y. Seo, A. Ummadisingu, S. M. Zakeeruddin, J. P. Correa-Baena, W. Tress, A. Abate, A. Hagfeldt, and M. Grätzel, Incorporation of rubidium cations into perovskite solar cells improves photovoltaic performance, *Science* **354**, 206 (2016).
- [61] Input file available at [https://github.com/barnesgroupICL/Driftfusion/blob/2022-EA\\_SDP\\_EIS/Input\\_files/spiro\\_mapi\\_tio2\\_2022\\_EA\\_SDP\\_EIS.csv](https://github.com/barnesgroupICL/Driftfusion/blob/2022-EA_SDP_EIS/Input_files/spiro_mapi_tio2_2022_EA_SDP_EIS.csv). Repository: [https://github.com/barnesgroupICL/Driftfusion/tree/2022-EA\\_SDP\\_EIS](https://github.com/barnesgroupICL/Driftfusion/tree/2022-EA_SDP_EIS). List of commands: <https://github.com/barnesgroupICL/Driftfusion/wiki/2022-ElectroAbsorbance,-Step-Dwell-Probe-and-EIS-on-heterojunction-model>.